# Multiwavelength, aerosol lidars at Maïdo supersite, Reunion Island, France: instruments description, data processing chain and quality assessment

Dominique Gantois[1], Guillaume Payen[2], Michaël Sicard[1], Valentin Duflot[1,3], Nelson Bègue[1], Nicolas Marquestaut[2], Thierry Portafaix[1], Sophie Godin-Beekmann[4], Patrick Hernandez[2], Eric Golubic[2].

[1] LACy, Laboratoire de l'Atmosphère et des Cyclones (UMR 8105 CNRS, Université de La Réunion, Météo-France), Saint-Denis de La Réunion, France
[2] Observatoire des Sciences de l'Univers de La Réunion (OSU-Réunion), UAR3365, Université de La Réunion, CNRS, IRD, Météo-France, 97490 Saint-Denis de La Réunion, France
[3] now at: Department for Atmospheric and Climate Research, NILU – Norwegian Institute for Air Research, Kjeller, Norway
[4] LATMOS, Laboratoire Atmosphères, Observations Spatiales, UPMC, Paris, France

*Correspondence to* : Dominique Gantois (Dominique.gantois@univ-reunion.fr)

**Abstract.** Understanding optical and radiative properties of aerosols and clouds is critical to reduce uncertainties in climate models. For over 10 years, the Observatory of Atmospheric Physics of La Réunion (OPAR, 21.079°S, 55.383°E) has been operating three active lidar instruments (named Li1200, LiO3S and LiO3T) providing time-series of vertical profiles from 3 to 45 km of the aerosol extinction and backscatter coefficients at 355 and 532 nm, as well as the linear depolarization ratio at 532 nm. This work provides a full technical description of the three systems, details about the methods chosen for the signal preprocessing and processing, and an uncertainty analysis. About 1737 night-time averaged profiles were manually screened to provide cloud-free and artifact-free profiles. Data processing consisted in Klett inversion to retrieve aerosol optical products from preprocessed files. The measurement frequency was lower during the wet season and the holiday periods. There is a good correlation between the Li1200 and LiO3S in terms of stratospheric Aerosol Optical Depth (AOD) at 355 nm (0.001-0.107; R = 0.92 ± 0.01), and with the LiO3T in terms of Angström exponent 355/532 (0.079-1.288; R = 0.90 ± 0.13). The lowest values of the averaged uncertainty of the aerosol backscatter coefficient for the three time-series are 64.4 ± 31.6 % for the LiO3S, 50.3 ± 29.0 % for the Li1200, and 69.1 ± 42.7 % for the LiO3T. These relative uncertainties are high for the three instruments because of the very low values of extinction and backscatter coefficients for background aerosols above Maïdo observatory. Uncertainty increases due to Signal to Noise Ratio (SNR) decrease above 25 km for the LIO3S and Li1200, and 20 km for the LiO3T. The Lidar Ratio (LR) is responsible for an uncertainty increase below 18 km (10 km) for the LiO3S and Li1200 (LiO3T). The LiO3S is the most stable instrument at 355 nm due to less technical modifications and less misalignments. The Li1200 is a valuable addition to fill in the gaps in the LiO3S time-series at 355 nm or for specific case-studies about the middle and low troposphere. Data described in this work are available at https://doi.org/10.26171/rwcm-q370 (Gantois et al., 2024).

## 1. Introduction

Uncertainties concerning aerosol and cloud optical and radiative properties strongly affect surface climate and also the accuracy in climate models (Hansen et al., 1997; Alexander et al., 2013). Aerosols can be of multiple origins, compositions, sizes, and shapes, but can also interact at different temporal and spatial scales and be influenced by various dynamical processes. This makes their observation at the global scale and the modelling of their properties challenging. Improving our knowledge in this area implies to use different measurement techniques (in situ, active and passive remote sensing methods) synergistically and to provide continuous timeseries of high-resolution measurements in the low and middle atmosphere.

The Observatory of Atmospheric Physics of La Réunion (OPAR), located on Réunion Island near Madagascar, is currently equipped with more than 50 instruments distributed over three different sites: two historical coastal sites in the north, and a high-altitude site (Maïdo observatory, 2160 m asl, Baray et al., 2013), which now houses more than two-thirds of these instruments. OPAR is part of many international networks, including GAW (Global Atmospheric Watch), NDACC (Network for the Detection of Atmospheric Composition Change), SHADOZ (Southern Hemisphere Additional OZonesondes), and AERONET (Aerosol Robotic Network). Additionally, it is a part of the European research infrastructures ACTRIS (Aerosol, Clouds, and Trace Gases Research Infrastructure) and ICOS (Integrated Carbon Observing System).

Maïdo observatory (21.079°S, 55.383°E) is one of the very few active observational sites in the Southern Hemisphere (SH). It is barely influenced by anthropic aerosols. Its importance lies in the fact that the aerosol load in the atmosphere above Reunion Island is under the influence of many different sources of emission and dynamical processes responsible for short and long-range air-mass transports (Baray et al., 2013) such as biomass burning (BB) plumes (Edwards et al., 2006; Khaykin et al., 2020), which are emitted seasonally in the SH. Moreover, it is not rare for volcanic aerosols to be detected in the stratosphere above Maïdo observatory. In fact, several volcanoes are located at the same latitude (Hunga-Tonga), or in the same Hemisphere (Calbuco) as Reunion Island (Bègue et al., 2017; Khaykin et al., 2017; Tidiga et al., 2022; Baron et al., 2023; Sicard et al., 2024). The high altitude of this facility is also of great importance as it is located above the boundary layer during the night, allowing the observation of the free troposphere in a quasi-pristine environment.

Since its creation in 2012, the Maïdo facility has been equipped with four research lidar (light detection and ranging) instruments emitting electromagnetic radiations at different wavelengths. Three of them have been providing high resolution time series of aerosol extinction and backscatter vertical profiles in the UV (355 nm) and visible (532 nm) domains. As of today, these measurements have only been used occasionally for case studies (Bègue et al., 2017; Khaykin et al., 2017; Tidiga et al., 2022; Baron et al., 2023; Sicard et al., 2024). Full exploitation of these timeseries will enable to provide timeseries of aerosol extinction and backscatter profiles over Reunion Island. This can only be achieved after homogenizing the processing method for the three instruments.

This works provides a summary of the specifications of the systems and a full description of the preprocessing and processing methods used to produce different levels of the datasets for the three Maïdo lidars.

## 2. Instrumental description

**Table 1** is a summary of the characteristics of the three Maïdo lidars used to retrieve aerosol optical properties. A full description of each system is available in the following subsections.

| | Li1200 | | LiO3S | LiO3T | | |
|---|---|---|---|---|---|---|
| **References** | (Dionisi et al., 2015; Vérèmes et al., 2019) | | (Portafaix et al., 2015) | (Duflot et al., 2017) | | |
| **Time-series** | In 2013-2017 | 2017-ongoing | 2013-current | In 2013-2017 | 2017-ongoing | |
| **Laser** | 2 × Quanta-Ray Nd: YAG pro-290 | | 1 × Quanta-Ray Nd: YAG Lab-150 | 1 × Quanta-Ray Nd: YAG Pro-290 | | |
| **Emitted wavelength (nm)** | 355 | | 355 | 532 | 1064 | |
| **Frequency (Hz)** | 30 | | 30 | 30 | | |
| **Energy (mJ/pulse)** | 375 | | 150 | 250 | | |
| **Reception channels (nm)** | Elastic 355M, 355H Raman 387 | Elastic 355VL, 355L Raman 387L | Elastic 355H, 355M Raman 387M | Elastic $532_{//}$, $532_\perp$ | Elastic 532H, 1064 Raman 607 | |
| **Telescope diameter (mm)** | 1 × 1200 | + 1 × 200 | 4 × 500 | 1 × 200 | + 1 × 500 | |
| **Full overlap (km)** | ~ 15 | ~ 15 | ~ 4-5 | ~ 4-5 | ~ 4-5 | |
| **Detectors** | Hamamatsu Photomultiplier tube (PMT) | | Hamamatsu PMT | Hamamatsu PMT | Photodiode (1064nm) | |
| **Detector mode** | Photocounting | | Photocounting Analog (355M) | Photocounting Analog (532H, 1064) | | |
| **Filter bandwidth (nm)** | 1 | 1.3 (355VL) 1.3 (355L) 3 (387L) | 1 | 1 | 0.7 (532H) 1.6 (607.7) *4 (1064)* | |
| **Raw vertical resolution (m)** | 15 | | 120 (2012 → 2017) 15 (2017 → current) | 7.5 | | |
| **Acquisition** | Licel transient recorders | | | | | |
| **Raw files integration time (minute)** | 1 | | 3 (2012 → 2017) 1 (2017 → 2022) | 2 | | |
| **Reception channels (nm)** | 355H, 355M, 387 | + 355L, 355VL + 387VL | 355H, 355M, 387 | Elastic // 532 Elastic ⊥ 532 | + 532H | + 607.7 *+ 1064* |
| **Observation capabilities (Range, km)** | 15-45 | 3-25 | 10-45 | 4-25 | 10-45 | 4-15 |

**Table 1: Systems technical features. The letters VL, L, M and H after the wavelength stand for Very Low, Low, Medium and High, respectively. Only aerosol channels are listed here.**

## 2.1. Lidar 1200 (Li1200)

The Li1200 is a Rayleigh Raman lidar able to measure vertical profiles of temperature between 30 and 100 km asl and water vapor ratio from the ground up to 18 km (Vérèmes et al., 2019). Vertical profiles of aerosol light extinction and backscattering can also be retrieved from the raw signals, as this instrument provides Rayleigh-Mie scattering at 355 nm and Raman $N_2$ scattering at 387 nm. This instrument has been operating at the Maïdo facility since 2012 and produces data since 2013.

*(i)    Actual configuration*

**The emission** consists in two Nd: YAG lasers Pro-290, Quanta-Ray Pro Series, from Spectra-Physics, emitting electromagnetic pulses at 1064 nm and 30 Hz (https://www.laserlabsource.com/files/pdfs/solidstatelasersource_com/product-305/Nd_Yag_Laser_Nanosecond_Laser_1064nm_1250mJ_Spectra_Physics-1462086952.pdf). The final

wavelength emitted is 355 nm, which corresponds to the third harmonic of the initial wavelength. Each pulse delivers 375 mJ in 9 ns. The optical design of this lidar is represented in **Figure 1**. The two laser beams are recombined through a polarizer cube, then sent to the telescope through a series of mirrors. It should be noted that the lasers and the telescope are not in the same room, hence the use of many mirrors. BE1 and BE2 lenses form an afocal of magnification 1.25, reducing the divergence of the beams and mixing the phases. The goal is to reduce the hot spots, especially on the very fragile optic BE3. Last, the laser beam is channeled through the center of the main telescope and magnified by a factor of 10 thanks to the afocal system BE3 and BE4. The emission and main reception are therefore static coaxial, reducing the parallax effect and the minimum overlap altitude.

**The reception** is made of two telescopes. The main telescope consists in a primary mirror of 1200 mm diameter (M1200), which gave its name to this instrument. A secondary mirror HM sends the beam to the detection system. The L1 lens allows the beam to converge faster, which explains the 3.6 m value of the focal length. GS1 is a glass plate that sends about 8 % of the beam on the 355 nm Very Low (355VL channel) detector. As this detector is located before the FD2 diaphragm, its field of view is the same as the one of the telescope, and it receives signal in the very near-range. A density (ND) was placed in front of this detector to avoid saturation. FD2 is a diaphragm, located at the focal plane of the telescope. Its aperture improves the geometrical factor of the telescope for the detectors following it. DM1 is a dichroic filter that reflects 355nm and allows 387nm and 407nm to pass through. GS2 is a glass plate that sends about 8% of the beam on the 355 nm Medium (355M) channel and 92% of the beam on the 355nm Hight (355H) channel. DM3 is a dichroic filter which selects the 387 nm for the Raman N2 channel. As of 2017, a second telescope, with a 200 mm M200 primary mirror and a focal length of 1 m, sends the signal to a second detection box, using an optical fiber. This detection box filters the Rayleigh and Raman signals and channels them respectively to the 355L and 387L detectors.

All the **detectors** are photomultiplier tubes (PMT) from Hamamatsu, reconditioned by the Licel company (https://www.hamamatsu.com/content/dam/hamamatsu-photonics/sites/documents/99_SALES_LIBRARY/etd/PMT_TPMZ0002E.pdf). The 355H, 355M, and 355L detectors are electronically shuttered to prevent saturation. The **acquisition** cards also come from Licel and operate in photocounting mode. There are no analog channels. Raw files follow a 1-minute integration.

**To summarize**, 355M and 355H channels exist since 2013, but their acquisition starts at 15 and 25 km, respectively, to avoid saturation. Hence, the 355VL and 355L channels were added in 2017 to cover the first altitude ranges below 15 km. The minimum height for 355L electronic shuttering is 450 m asl.

*(ii)    Previous modifications*

The detection unit was modified in 2017. Before that, the detection unit containing the 355L and 387VL detectors did not exist. The M1200 mirror separation unit was modified. First, the part containing the FD1 to L3 optics, as well as the 355VL detector, did not exist. And there was an optic between IF2 and DM2 that would sen3d the visible signal to another detection unit. Indeed, originally, this lidar was supposed to operate at two emission wavelengths, 355 and 532nm. However, during installation, due to mechanical and optical problems, only the 355 nm channel was retained (Dionisi et al., 2015).
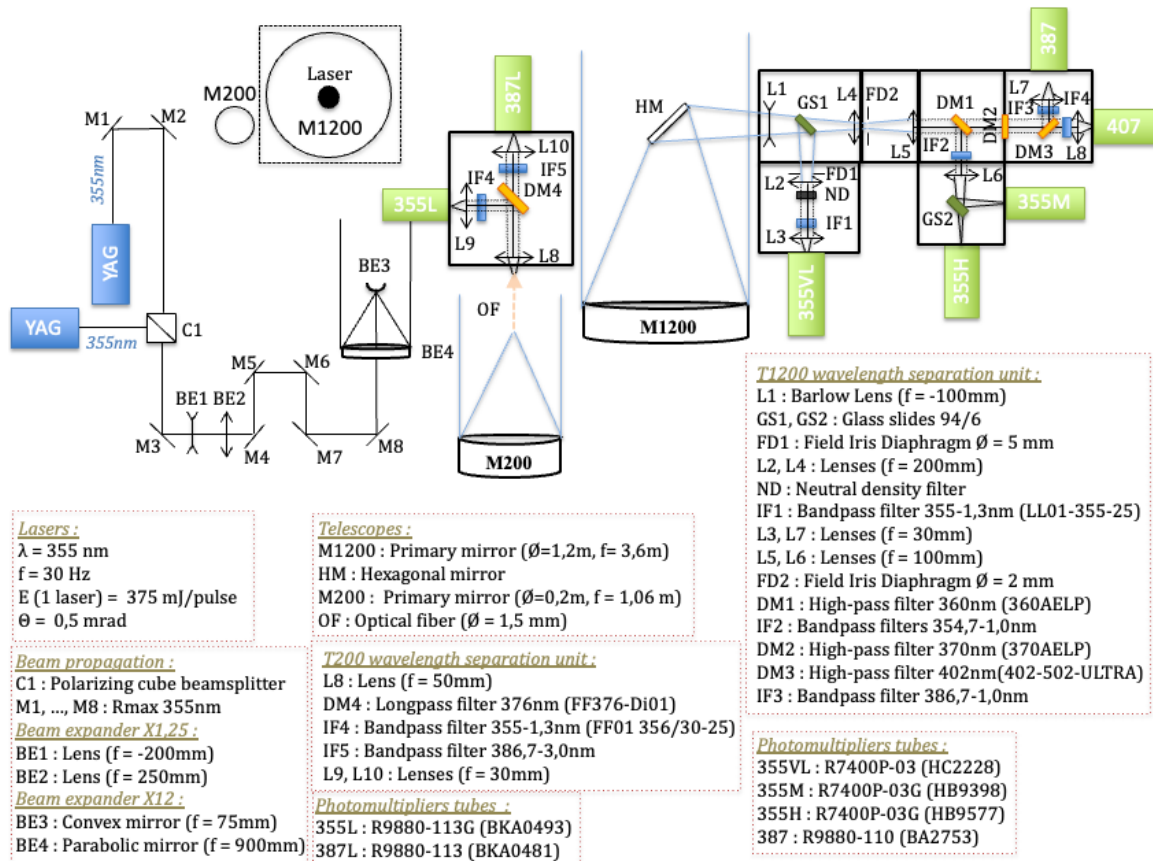
**Figure 1 : Li1200 optical scheme**

## 2.2. Stratospheric Ozone Lidar (LiO3S)

The Stratospheric Ozone Lidar (LiO3S) works with the DIfferential Absorption Lidar (DIAL) technique and provides vertical profiles of ozone ($O_3$) concentration in the stratosphere, between the tropopause and about 45 km (Godin-Beekmann et al., 2003; Portafaix et al., 2003). To this end, two different wavelengths are emitted: a 308 nm signal strongly absorbed by ozone molecules and a 355 nm signal weakly absorbed by ozone molecules. Vertical profiles of aerosol light extinction and backscattering can be retrieved from the elastic scattering at 355 nm and Raman $N_2$ scattering at 387 nm. From 2000 to 2012, the LiO3S was located at the Moufia University campsite in Saint-Denis and provided ozone vertical profiles. It was moved to the Maïdo facility in 2012 and has been measuring from this location since 2013.

### (i) Actual configuration

**The emission** set-up consists in two different lasers. An excimer laser IPEX-840, PulseMaster PM-800 Series excimer laser with XeCl gas from LightMachinery (https://lightmachinery.com/lasers/excimer-lasers/ipex-800/), emits electromagnetic pulses at 308 nm with a frequency of 40 Hz and pulse energy of 220 mJ. A Nd: YAG laser Lab-150, Quanta-Ray Lab Series from Spectra-Physics emits electromagnetic pulse at a 1064 nm with a frequency of 30 Hz (https://www.laserlabsource.com/files/pdfs/solidstatelasersource_com/product-305/Nd_Yag_Laser_Nanosecond_Laser_1064nm_1250mJ_Spectra_Physics-1462086952.pdf). The final wavelength emitted by the Nd: YAG laser is 355 nm, corresponding to the third harmonic of the emitted wavelength. The pulse energy at this wavelength is 130 mJ. The laser beam diameter is about 10 mm, and its divergence is 0.5 mrad. The optical design of this lidar is represented in **Figure 2**. Again, the emission and reception

5

149 of this lidar are located in different rooms, explaining the use of many mirrors. The expander consists in three
150 lenses, BE1, BE2 and BE3, magnifying the signal by a factor 10. The final beam has a 100 mm diameter.

151 **The reception** is made of four 500 mm diameter telescopes. The primary mirrors are M1, M2, M3 and M4.
152 The signal is emitted at the center of these telescopes, and the distance between the emission and the center of each
153 telescope is 600 mm. At the receiving end, the signal is a focused from each telescope to a corresponding optical
154 fiber, which are positioned in line before entering the detection box. In this box, a diffraction grating separates the
155 different wavelengths. Internal mirrors allow the beam to be reflected in the detectors. Finally, a glass plate
156 discriminates the high and low energy channels at 355 nm.

157 All the **detectors** are photomultiplier tubes (PMT) from Hamamatsu, reconditioned by the Licel company
158 (https://www.hamamatsu.com/content/dam/hamamatsu-
159 photonics/sites/documents/99_SALES_LIBRARY/etd/PMT_TPMZ0002E.pdf), and the signal **acquisition** cards
160 are from Licel. The 355 nm detectors are electronically shuttered to avoid saturation. The acquisition is in
161 photocounting mode only for the high energy channels, and in photocounting and analog mode for the low energy
162 channels. Raw files follow a 1minute integration.

163 *(ii)     Previous modifications*

164 Before 2017, the electronic obturation concerned only 355H and 308H channels, and a mechanical chopper
165 shuttered 355M, 308M and Raman channels at the entrance of the detection box. In 2017, this chopper
166 malfunctioned and was replaced by electronic obturation for the 355M and 308M channel. Raman channels were
167 not shuttered anymore. The initial integration time was 3 minutes and was reduced to 2 and then 1 minute. During
168 this period, the vertical resolution was modified from 120 m to 15 m.
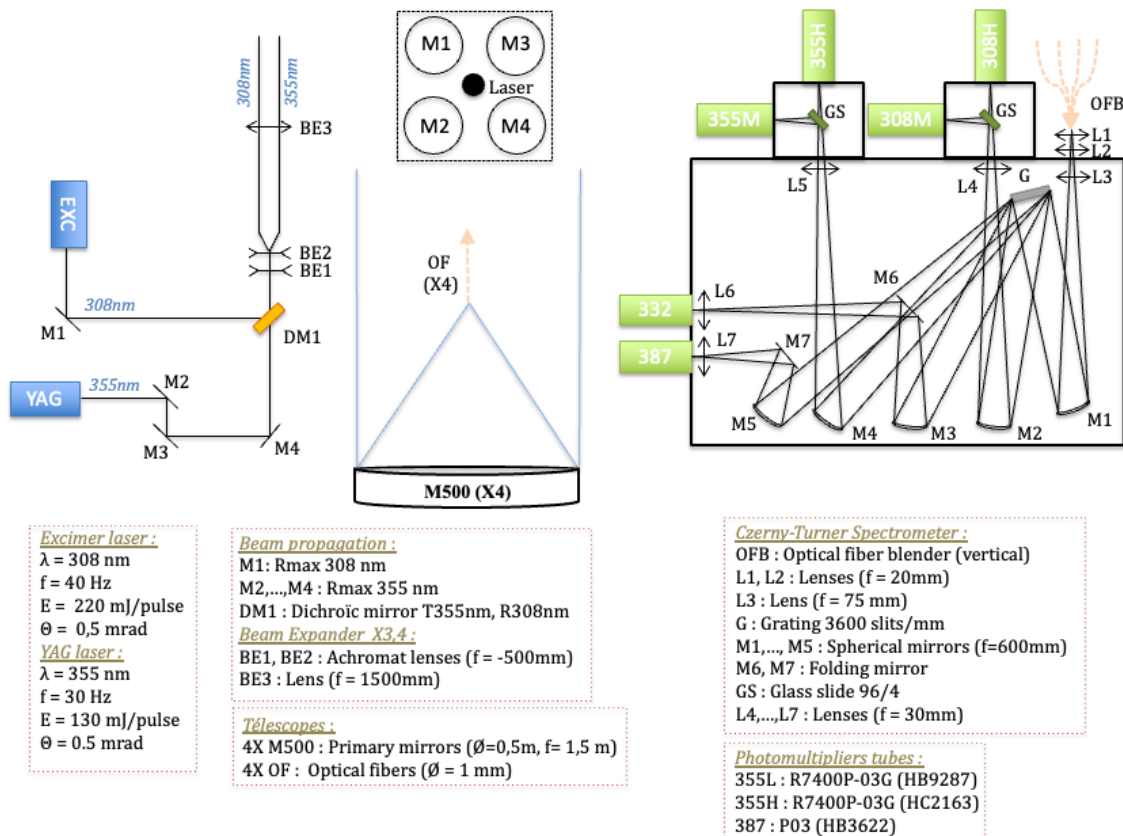


169

**Figure 2 : LiO3S optical scheme**

170

## 2.3. Tropospheric Ozone Lidar (LiO3T)

The Tropospheric Ozone Lidar (LiO3T) also works with the DIAL technique and provides vertical profiles of ozone ($O_3$) concentration in the troposphere, between 6 and 25 km (Duflot et al., 2017). To this end, two different wavelengths are emitted using stimulated Raman scattering: a 289 nm signal strongly absorbed by ozone molecules and a 316 nm signal weakly absorbed by ozone molecules. Vertical profiles of aerosol light extinction and backscattering can be retrieved from the residual emission of the laser in terms of elastic scattering at 532 nm and 1064 nm, and Raman $N_2$ scattering at 607 nm. From 1993 to 2012, the LiO3T was located at the Moufia University campsite in Saint-Denis and provided ozone vertical profiles. It was moved to the Maïdo facility in 2012 and has been measuring from this location since 2013. The first aerosol dedicated polarized channels were installed in 2014.

*(i)     Actual configuration*

**The emission** consists in a Nd: YAG lasers Pro-290, Quanta-Ray Pro Series, from Spectra-Physics, emitting initially at 1064 nm at 30 Hz (https://www.laserlabsource.com/files/pdfs/solidstatelasersource_com/product-305/Nd_Yag_Laser_Nanosecond_Laser_1064nm_1250mJ_Spectra_Physics-1462086952.pdf). While the fourth harmonic (266 nm) is used to retrieve tropospheric ozone profiles (through its passage in a Raman cell generating 289 and 316 nm pulses), we use the second harmonic (532 nm) to retrieve aerosol light extinction and backscattering. Each pulse at 532 nm provides an energy of 250 mJ. The laser beam diameter is of about 10 mm, and its divergence is about 0.5 mrad. The optical design of this lidar for aerosol measurements is represented in **Figure 3**. Again, the emission and reception of this lidar are located in different rooms, explaining the use of many mirrors. The lenses, BE1, BE2 and BE3, magnify the signal by a 15 factor. The final emitted beam diameter is 100 mm.

**The reception** is made of two telescopes: one for the Rayleigh and Raman channels (532, 607 and 1064 nm, respectively), and the other for the polarized channels at 532 nm. The first telescope (M500) consists in a 500 mm diameter primary mirror. An optical fiber located at its focal point, conducts the signal to the detection box. Dichroic filters separate the 532, 607 and 1064 nm wavelengths. The second telescope consists in a 200 mm diameter primary mirror immediately followed by a polarizing cube. An optical fiber leads the polarized and cross-polarized beams to interference filters and to the detectors.

All the **detectors** are photomultiplier tubes (PMT) from Hamamatsu, reconditioned by the Licel company (https://www.hamamatsu.com/content/dam/hamamatsu-photonics/sites/documents/99_SALES_LIBRARY/etd/PMT_TPMZ0002E.pdf), except for the 1064 nm detector, which is an avalanche diode with a 3 mm diameter sensor (https://www.hamamatsu.com/content/dam/hamamatsu-photonics/sites/documents/99_SALES_LIBRARY/ssd/si_apd_kapd0001e.pdf). The 532 high energy channel (532H) detector is the only one electronically shuttered. All the **acquisition** cards are from Licel. The acquisition of the 532 nm polarized channel as well as the 607 nm channel are in photocounting mode. The acquisition of the 532H channel is in photocounting and analog modes, and the acquisition of the 1064nm channel is only in analog mode. Raw files follow a 2-minute integration.

*(ii)     Previous modifications*

208 In 2014, the 200 mm telescope (M200) and the T200 wavelength separation unit were installed, allowing for the
209 first aerosol measurements with polarized channels.  In 2017, one of the four 500 mm telescopes initially dedicated
210 to ozone measurements was used for aerosol measurements. A second detection box was added, enabling the 607
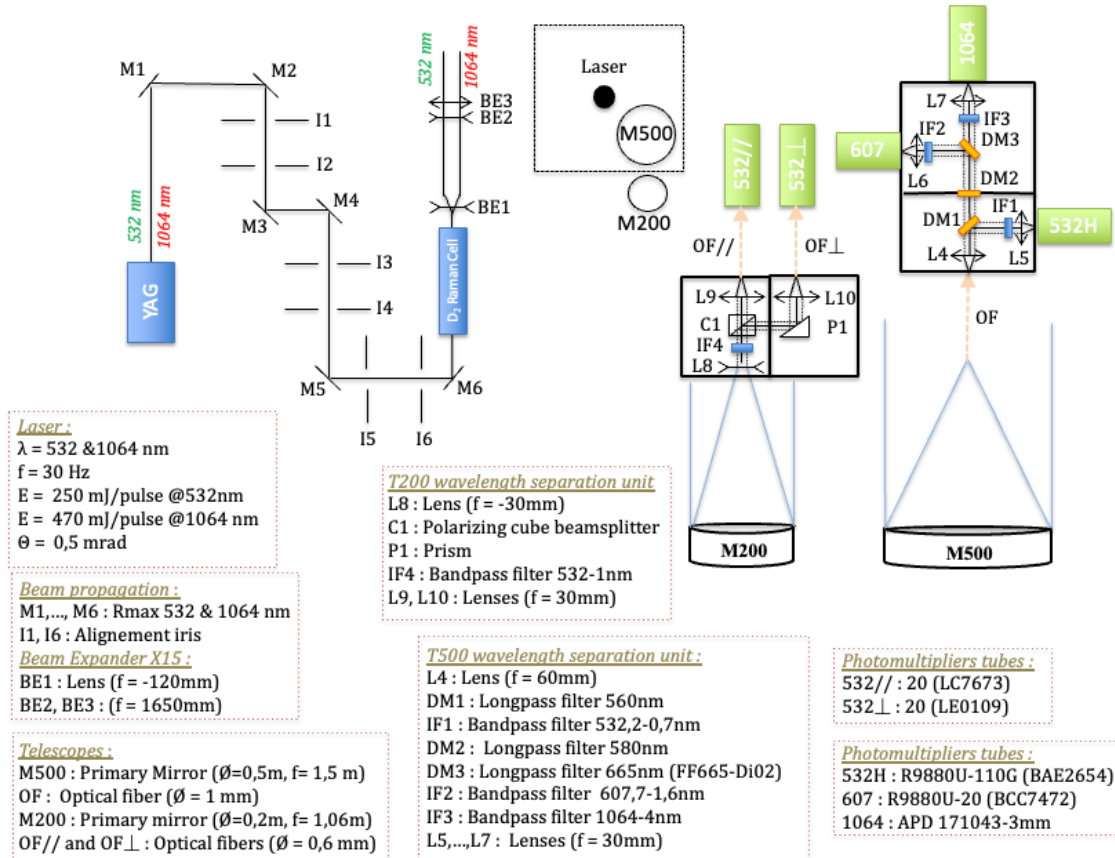211 nm and 1064 nm channels acquisition.



212

**Figure 3 : LiO3T optical scheme**
213

## 3.  Routine measurements

214

215    The Maïdo lidars are research instruments that require manual handling and a constant human presence while
216 operating. Maïdo observatory is a high-altitude facility (2160 m asl) and is located above the boundary layer in the
217 free troposphere during the night. Acquisitions are only made during the night to increase the SNR. These
218 instruments were originally intended to observe data in the stratosphere and the upper troposphere, so they are
219 optimized to work at night, to improve the SNR up to very high in the atmosphere. That is why acquisitions are
220 only made during the night. Measurements also require the absence of low-clouds or rain. The position of the
221 Maïdo observatory on the west side of Reunion Island often protects the site from the clouds brought by trade
222 winds. Notably, a ceilometer was installed at the Maïdo facility in 2019 and continuous observations revealed an
223 average cloud frequency of respectively 20% and 40% during winter and summer nights (not shown).

224    Routinely, Maïdo lidars are operated two nights per week and measurements last from 7pm to 1am (local time,
225 i.e. from 15 to 21 UTC). Specific campaigns (once or twice a year) can occasionally require to significantly
226 increase the number of measurements. Operating these instruments implies to follow a strict, well-prepared
227 protocol including basic check-ups and laser power control. A metadata file is routinely fed with technical specifics

228 for each night of observation and after any instrumental modification. Automatization is currently in progress and
229 could increase the frequency of routine measurements.

230 Maïdo lidars are large and cannot be moved to make horizontal measurements: the beams of the different lidars
231 are always vertical. To avoid any problems with flying objects, a no-fly zone around the Observatory is requested
232 before each lidar measurement and during operating hours (exclusively nighttime). The research building hosting
233 these instruments has a restricted access. It is located far from any residential areas. The instruments themselves
234 can only be accessed by trained authorized personnel equipped with personal protective equipment (including eye
235 protection glasses for the laser wavelengths) and Optical Enclosures.

236

## 4. Data processing chain

### 4.1. Data processing levels

Our datasets follow a classification detailed in the following description. Data processing levels range from Level 0 to Level 2.

**(i)** Level 0 products ($L_0$) are uncorrected and uncalibrated raw data files in Licel format at full resolution produced by the instrument.

**(ii)** Level 1 products ($L_1$) provide cloud-free data cleaned from any instrumental artifact (electronic parasites, synchronization problems, power disrupt, etc.). The cloud mask is currently manual. These corrections are essential for any user to be able to apply their own specific aerosol preprocessing without errors linked to the instrument itself or the weather.

**(iii)** Level 2 products ($L_2$) provide processed lidar data including: saturation correction, background-sky correction, geometrical form factor correction and gluing between high and low-energy channels. These products also provide the aerosol optical properties and their corresponding uncertainties.

### 4.2. $L_0$ to $L_1$ processing chain

Each instrument is equipped with an acquisition system provided by the Licel firm. The description of the acquisition program producing output files in Licel format can be downloaded at *http://licel.com/raw_data_format.html*. This process concerns three main sources of interferences: **(i)** Detection-related interferences, **(ii)** Acquisition problems and **(iii)** Interferences linked to the lidar environment.

Any significative step of this process is tagged in the L1a output files to identify the corrections applied.

### 4.2.1. Detection interferences

Detection-related interferences can generally be linked to electromagnetic disturbances, which can occur in three different ways.

**(i)** An increased background signal concerning variable altitude ranges can impact the complete profile as shown in **Figure 4a**. This disturbance affects one or several channels across a significant altitude range, making the data acquisition unusable and requiring its withdrawal. The strong disturbance in the signal made it easy to fully automatize their detection. Notably, obturated detectors are more sensitive to these disruptions. Experience proved that they are directly related to the use of cell phones and Talky-Walkies. These instruments have been

267 banned from the instrumental rooms during the measurements, significantly decreasing the frequency of these
268 cases.

269 **(ii)** A second electronic problem often encountered comes from electronic gating. In fact, if a high and low-
270 energy channel coexist, a peak can be observed on the low-energy channel raw signal, at the gated altitude of the
271 high-energy channel (**Figure 4b**). This parasite peak usually appears on 2 consecutive range bins. This type of
272 problem occurs when the detectors are obturated and can have a significant impact on the measurement. It is
273 therefore necessary to remove the corresponding values and replace them by an averaged value between the
274 previous and following range bins.

275 **(iii)** The third detection disturbance corresponds to a sudden peak of the signal on a single randomly located
276 range bin. They only concern LiO3S and LiO3T. The consequence on the nighttime averaged profile is shown on
277 **Figure 4c**. Generally, the intensity of these spurious peaks is consistent and significantly higher than the
278 atmospheric background noise. They are easily identified when the intensity of the received signal is much lower
279 and become negligible with a stronger signal. However, there is an intermediate zone where the intensity of the
280 received signal is close to the intensity of these peaks, making their detection more challenging. They are replaced
281 by an averaged value.
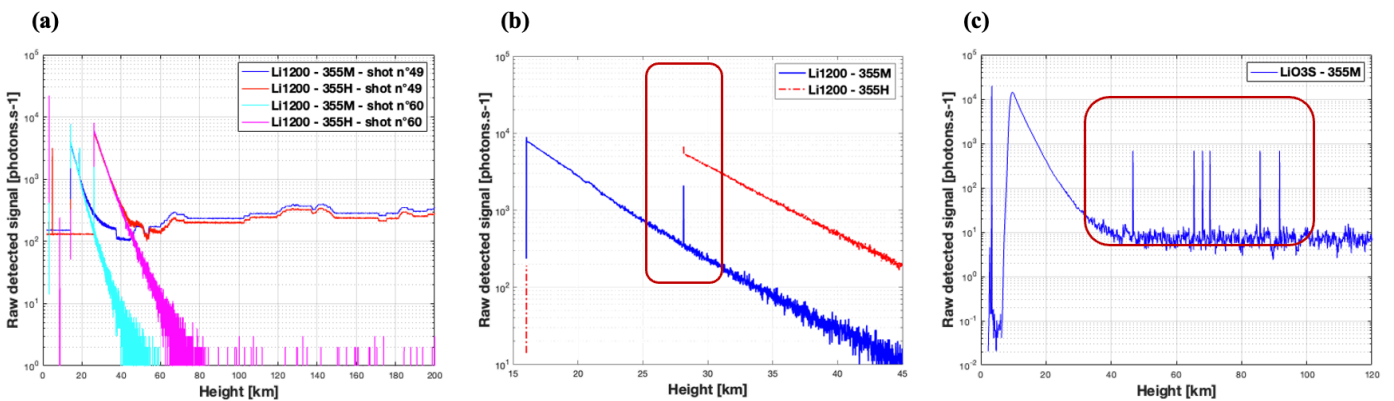


**Figure 4: (a) Raw Li1200 signal: background signal anomaly, (b) Raw Li1200 signal: peak from electronic gating, (c) Raw**
283 **LiO3S nighttime averaged signal: random peaks in the far-range.**

### 4.2.2. Acquisition problems

285 The acquisition program computes 1- or 2-minute integrated profiles, depending on the instrument. However,
286 with this acquisition program, the measurement cannot be stopped at the end of the current cycle. As a result, the
287 last file is generally shorter than the others and must be removed to guarantee consistent measurements.

288 Another issue was a time desynchronization of several minutes between the computer acquisition clocks in
289 2021, revealing a configuration default in the corresponding Network Time Protocol time servers. Time differences
290 could increase up to 15 minutes between the different computers. This default has been fixed and a time-correction
291 is applied for signals between 2012 and 2021.

292 Last, interaction between the different lidars working at the same time and emitting the same wavelength can
293 also lead to interferences and disturbances on sensitive channels. To avoid this issue, the lasers are synchronized
294 out of phase. However, errors with this offset can lead to files with a higher sky background than others. These
295 files are removed.

### 4.2.3. Disturbance from clouds.

297     The SNR is most sensitive to the presence of low-altitude clouds. These clouds strongly absorb the emitted
298     photons and lead to high extinction levels and weak SNRs. They must be removed. High-altitude cirrus clouds can
299     also be removed if stratospheric aerosols are studied. Cloud-detection can be both automatic and/or manual. An
300     automatic detection of low clouds under 5 km height has been developed and can be used from 2019 up to now
301     using data from a Campbell CS135 ceilometer set up at the Maïdo facility in 2019. A manual cloud screening is
302     done for any remaining cirrus or low clouds. Automatization is in progress for this time-consuming work.

### 4.3.      $L_1$ to $L_2$ processing chain

304 The goal of this second processing chain is to retrieve vertical profiles of aerosol optical products. It involves
305 several key steps.

### 4.3.1.      Saturation correction

307     Saturation affects photomultiplier tube detectors with an acquisition card in photocounting mode. It concerns
308 the lower layers of the atmosphere and appears when the number of backscattered photons overcomes the capacity
309 of the acquisition card to discriminate them individually. Therefore, the backscattered signal is attenuated in the
310 corresponding layers. On the contrary, acquisition in analog mode is not affected by saturation, but has a weaker
311 SNR.

312     One solution is to combine (namely glue) analog and photocounting channels if both are available, which is
313 not always the case for our instruments.

314     The second option is to compare high and low-energy channels (or analog and photocounting channels if
315 available) in the lower layers and apply a dead-time correction to the photocounting channel using the Müller
316 equation. This is the solution we adopted for Maïdo lidars concerning aerosol, which is similar to what is done
317 for ozone and temperature processings (Leblanc et al., 2016a; Leblanc et al., 2016b). The dead-time parameter
318 ($\tau_d$) corresponds to the minimum time for discriminating two consecutive photons. Our photocounting modes are
319 non-extensive, which means that the dead-time value is independent from the number of backscattered photons.
320 We then apply the Müller equation (Müller, 1973):

321
$$S_{desat} = \frac{S_{sat}}{1 - \tau_d \cdot \frac{c}{2 . \delta_z . L} \cdot S_{sat}} \quad (1)$$

322

323 With $S_{sat}$ (resp. $S_{desat}$) corresponding to the saturated (resp. desaturated) detected signal in number of photons
324 per second, $\delta_z$ the vertical resolution in meters, $c$ the light celerity in meters per second, and $L$ the number of shots.

325 A value of $\tau_d = 3.7 ns$ is chosen. This value is the one recommended by Licel manufacturers and was confirmed
326 after several experimental tests which are available in a summary document.

### 4.3.2.      Background correction

328     The background sky signal ($S_{BC}$), is one of the main sources of noise affecting the SNR. It corresponds to: **(i)**
329 the detector noise, and **(ii)** the natural light emitted by the atmosphere and can be affected by the presence of the
330 moon during the night. The value of this signal is supposed to be constant with the altitude but in practice it
331 sometimes follows a linear variation due to the effect of the signal induced noise on the detector. Our instruments
332 are not equipped with any pre-trigger. Our method to calculate the ($S_{BC}$) value consists in performing a linear

333 regression or an averaging of the desaturated signal in an altitude range high enough to neglect the impact of the
334 backscattered signal compared to the ($S_{BC}$), typically between 80km and 120km.

### 4.3.3. Geometrical form factor correction

336 The overlap function $F(z)$ or crossover function is one of the major sources of uncertainties for ground-based
337 lidar measurements. It describes the fraction of the laser beam cross section contained by the telescope field of
338 view as a function of range. Its values vary between 0 (blind zone, no overlap) and 1 (full overlap). Originally,
339 Maïdo lidars were designed to study the high troposphere and the stratosphere and at these altitudes, the full overlap
340 is obtained, which is why there has not yet been a more specific study on these instruments.

341 Should this parameter not be corrected, the received lidar signal would be attenuated between the blind zone
342 and the full overlap, leading to incorrect optical values. Two approaches can be followed to determine this
343 parameter. **(i)** A theoretical calculation using equations found in Measures (1984) can be performed. However, it
344 implies the knowledge of several optical parameters which can vary over the timeseries, and different equations
345 must be used for coaxial and biaxial systems. **(ii)** The second and most common approach is experimental and
346 implies the use of horizontal measurements (Chazette et al., 2017). In fact, considering a constant and homogenous
347 atmosphere along the line of sight, a linear regression can be performed in an altitude range high enough to be far
348 from the full overlap. The difference between the logarithm of the signal and this linear regression gives an accurate
349 estimation of $F(z)$.

$$F(z) = \exp\left(\ln\left(S_2(z)\right) - y(z)\right) \quad (2)$$

351 With $S_2$ the desaturated, background corrected, and range corrected lidar signal, $y(z)$ the linear regression and
352 $z$ the altitude range.

353 It is physically impossible for these research instruments to measure horizontally. Therefore, the experimental
354 approach using vertical measurements (instead of horizontal) in aerosol-free conditions was performed to correct
355 overlap for the very low and low channels of the lidar 1200. As of today, no overlap correction was needed for the
356 LiO3S (full overlap under 10km) and LiO3T (full overlap between 3 and 4km).

357 **Figures 5a and 6a** reveal the variability of the overlap function over the time-series for both Li1200 VL and
358 L channels. This variability can be explained by slight misalignments of the lidar. Indeed, given the important
359 number of optical elements between the laser and the emission point, the risk of misalignment, even minor, is
360 significant. **Figures 5b and 6b** show the mean and standard deviation (std) of the overlap function from an
361 exponential regression. The small values of std are an indicator of a low-varying function, a result that allows to
362 use a unique overlap function rather than different functions for different periods. The estimated altitude of full
363 overlap was 10 km for the Very Low channel and 15k m for the Low channel.
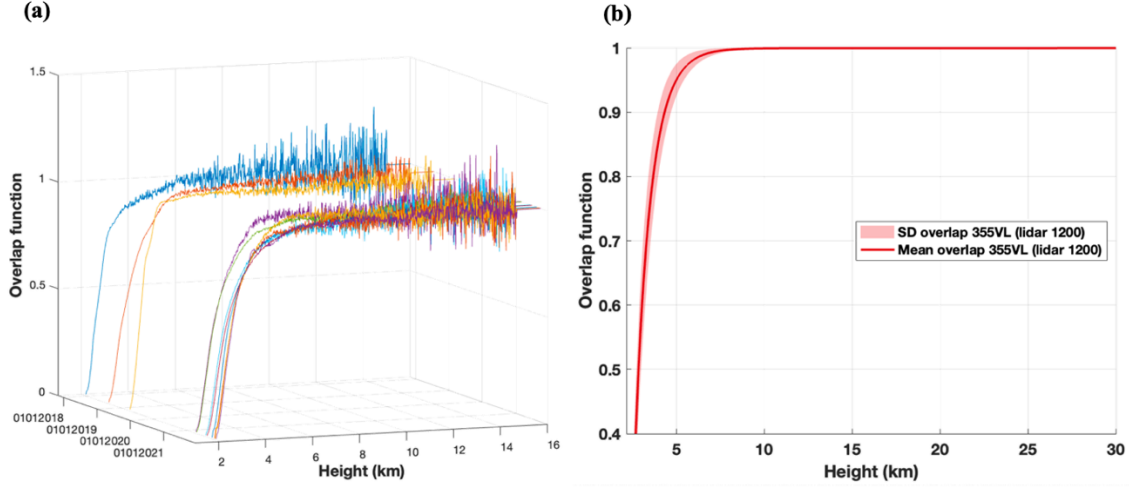
**Figure 5: Li1200 VL channel. (a) Time series of overlap functions, (b) Mean and standard deviation of the overlap function.**



**Figure 6: Li1200 L channel. (a) Time series of measured overlap functions, (b) Mean and standard deviation of the exponential regression of the overlap function.**
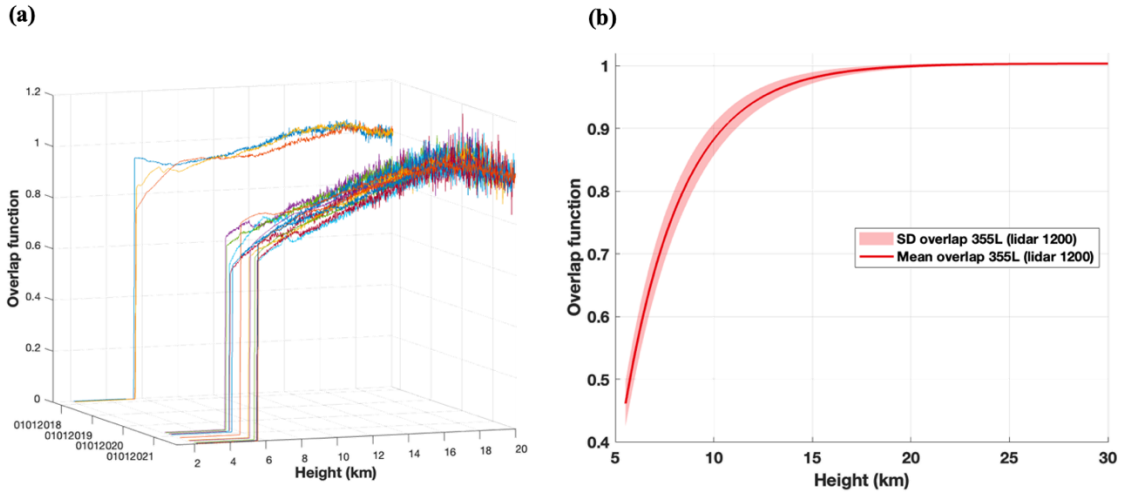
### 4.3.4. Smoothing

Smoothing is applied on the lidar signal to increase the accuracy of the retrieved aerosol profiles. For the three time-series, smoothing was achieved using a low-pass filter with a Blackman window (Blackman and Tukey, 1958). The number of points for the filter was altitude-dependent and channel-dependent.

$$S_{filt}(z) = S_2(z)/F(z) * \frac{coef}{\sum coef} \quad (3)$$

$$coef(n) = 0.42 - 0.5 * cos\left(\frac{2\pi n}{W-1}\right) + 0.08 * cos\left(\frac{4\pi n}{W-1}\right), 0 \leq n \leq M-1 \quad (4)$$

With $S_{filt}$ the smoothed signal, $S_2$ the desaturated, background corrected, and range corrected lidar signal, $M$ half the length of the window and $W$ the weight of the filter.

**Figures 7a-c** represent the new vertical resolution for each channel of each instrument. Two methods can be used to estimate vertical resolution after smoothing: **(i)** Impulse response method and **(ii)** Digital Filter. The latter was

13

379  chosen for these time-series. It involves the mathematical calculation of the filter transfer function, using a cut-off
380  frequency at -3dB (NDACC_resolDF, (Leblanc et al., 2016)).

381

382
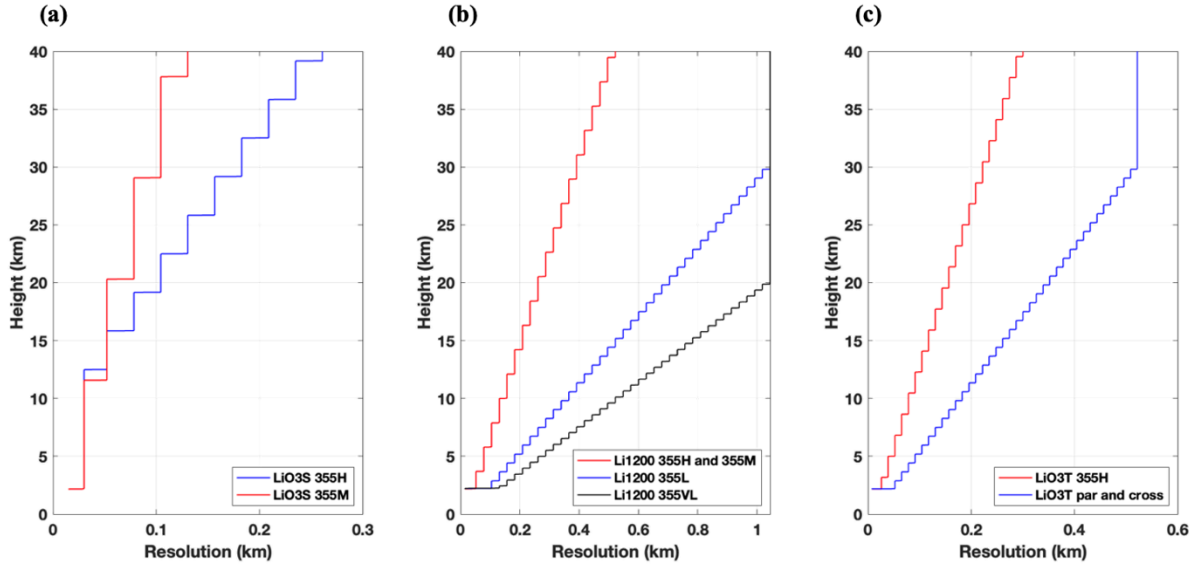


**Figure 7: NDACC vertical resolution of (a) LiO3S, (b) Li1200, and (c) LiO3T.**

### 4.3.5. Gluing near and far-range channels

High and low energy channels were combined for the LiO3S and the Li1200 using the gluing method of the square sinus and cosinus functions. The altitude range chosen for the gluing corresponded to a region where the high energy channel was not affected by electronic distortions and the low energy channel was not affected by too much noise.

$$\begin{cases} v1(z) = 0, & z < altmin \\ v1(z) = \sin^2\left(\frac{0 \xrightarrow{n} 1}{n} * \frac{\pi}{2}\right), & altmin \leq z \leq altmax \end{cases} \quad (5)$$

$$\begin{cases} v2(z) = 1, & z < altmin \\ v2(z) = \cos^2\left(\frac{0 \xrightarrow{n} 1}{n} * \frac{\pi}{2}\right), & altmin \leq z \leq altmax \end{cases} \quad (6)$$

With $n$ the number of range bins between $altmin$ and $altmax$, $v1$ the vector to apply to the high energy channel and $v2$ the vector to apply to the low energy channel.

The channels glued and used for inversion were: **(i)** 355VL + 355L + 355M + 355H and 355L + 355M + 355H and 355M + 355H for the Li1200, and **(ii)** 355H + 355M for the LiO3S. Each of these glued channels is available in the $L_{1b}$ files. Inversion was applied for each glued channels and corresponding optical products can be found in the $L_2$ files.

### 4.3.6. Calibration depolarization value for the LiO3T

Polarization channels enable to detect changes in the backscattered polarization state produced by the atmospheric particles. The laser provides quasi pure linear polarization. A polarizing cube beam splitter transmits

14

401    the received linear polarized light and reflects the received cross polarized light. It is necessary to determine the

402    polarization calibration factor before combining the two signals (Biele et al., 2000).

403    Three methods can be used: **(i)** Rayleigh calibration method (Behrendt and Nakamura, 2002), **(ii)** $\pm 45°$ or $\Delta 90°$

404    calibration methods (Freudenthaler, 2016), and **(iii)** 3 signals (total, cross and parallel) method (Reichardt et al.,

405    2003). While methods 2 and 3 provide the smallest uncertainties, method 1 can be used retrospectively if no total

406    channel existed. The apparent Volume Linear Depolarization Ratio (VLDR*) can then be calculated following:

407

408
$$VLDR^* = \frac{K}{\eta^*} * \frac{S_r}{S_t} \quad (7)$$

409

410    With $t$ and $r$ the respective transmitted and reflected parts of the signal $S$, $\eta^*$ the apparent calibration factor and $K$

411    the calibration factor correction parameter.

412    The VLDR can then be computed using the polarization crosstalk parameters for the transmitted and reflected

413    signals ($G_{t,r}$ and $H_{t,r}$):

414

415
$$VLDR = \frac{VLDR^*(G_t + H_t) - (G_r + H_r)}{(G_r - H_r) - VLDR^*(G_t - H_t)} \quad (8)$$

416

417    The total signal will also be reconstructed following:

418

419
$$S_{total} = \frac{\frac{\eta^*}{K} H_r S_t - H_t S_r}{H_r G_t - H_t G_r} \quad (9)$$

420

421    The aerosol backscatter $\beta_a$ will then be deduced from the total signal $S_{total}$ using Klett inversion. The backscatter

422    ratio $R$ will be calculated following:

423

424
$$R = \frac{(\beta_a + \beta_{mol})}{\beta_{mol}} \quad (10)$$

425

426    Finally, the Particle Linear Depolarization Ratio (**PLDR**) can be computed following:

427

428
$$PLDR = \frac{(1 + LDR_{mol}) * VLDR * R - (1 + VLDR) * LDR_{mol}}{(1 + LDR_{mol}) * R - (1 + VLDR)} \quad (11)$$

429

430    In our case, we used the Rayleigh method before 2017 and the 3 signals method after 2017. We used a linear

431    molecular depolarization ratio ($LDR_{mol}$) of 0.00398 at 532nm (Behrendt and Nakamura, 2002) to estimate $\eta^*$, and

432    a $K$ factor of 1 to estimate **VLDR***. Crosstalk parameter values were considered ideal: $G_t = 1$, $H_t = 1$, $G_r = 1$ and

433    $H_r = -1$.

434        **4.3.7.    Optical products: Klett inversion**

435     This step is mandatory to retrieve aerosol optical properties from the detected lidar signals. However, it implies
436 to resolve an order 1 Bernoulli equation with several unknown parameters. Several methods exist such as: (i) One
437 or two-components Klett inversion (Klett, 1981, 1985), (ii) Raman inversion (Ansmann et al., 1990, 1992), and
438 (iii) a synergistic method using Klett inversion and sunphotometer measurements to evaluate the lidar ratio (Raut
439 and Chazette, 2007).

440     Because Raman channels have currently a very low SNR, they are not included in this work and the two-
441 component Klett inversion method was chosen for the three systems. It implies to determine an *a priori* constant
442 value of Lidar Ratio (LR) and a clean, aerosol-free zone in the atmosphere (Rayleigh zone). Details about the
443 elastic two-component algorithm from Klett are available in **Appendix A**.

444 The solution proposed in Appendix A is:

445

446
$$\beta(\lambda, z) = \beta_a(\lambda, z) + \beta_m(\lambda, z) = \frac{S_2(\lambda, z).\exp\{2.\int_{z'=z}^{z_{ref}}\left(\frac{LR_a(\lambda, z')}{LR_m(\lambda, z')} - 1\right).\alpha_m(\lambda, z')dz'\}}{\frac{S_2(\lambda, z_{ref})}{\beta(\lambda, z_{ref})} + 2.\int_{z'=z}^{z_{ref}} LR_a(\lambda, z').S_2(\lambda, z').\exp\{2.\int_{x'=z}^{z_{ref}}\left(\frac{LR_a(\lambda, x')}{LR_m(\lambda, x')} - 1\right).\alpha_m(\lambda, x')dx'\}.dz'} \quad (12)$$

447

448     With $a$ (resp. $m$) the particular (resp. molecular) contribution, $\alpha(\lambda, z)$ (resp. $\beta(\lambda, z)$) the summed molecular and
449 particular extinction (resp. backscatter), and $LR$ the Lidar Ratio. $S_2$ corresponds to the range-corrected, sky
450 background corrected and desaturated signal. However, the signal used in this study for the inversion algorithm is
451 smoothed as explained in paragraph 4.3.4. and could be glued (Li1200, LiO3S) or recombined (LiO3T).

452 Several unknown parameters must be determined:

453     (i)     To retrieve the $LR_a$, we chose a constant LR value of 50 sr for the three instruments to be consistent
454           between the time-series and to target the most frequent aerosol types. Moreover it enables easier
455           comparisons with satellite data such as CALIOP products (Cattrall et al., 2005).

456     (ii)    The equation used to retrieve the molecular extinction was (Bates, 1984):

457
$$\alpha_m(\lambda, z) = \frac{P}{k * T} * \frac{4.02.10^{-28}}{\lambda^{4+(0.389\lambda+0.09426\lambda^{-1}-0.3228)}} \quad (13)$$

458           With $k$ corresponding to the Boltzmann constant. Atmospheric pressure $P$ and temperature $T$ were
459           retrieved from the Arletty AERIS product *(https://www.aeris-data.fr/)*, relying on data from the
460           European weather forecast model ECMWF (European Centre for Medium-Range Weather Forecasts),
461           and producing interpolated data every 6h around Maïdo observatory (Hauchecorne, n.d.).

462

463           The molecular backscatter was then computed following:

464

465
$$\beta_m(\lambda, z) = \alpha_m(\lambda, z) * \frac{3 * K_f}{8\pi} \quad (14)$$

466           The King factor's value ($K_f$) is considered equal to 1 (King, 1923), and $\frac{3}{8\pi}$ corresponds to the $LR_m$.

467     (iii)   The last step was to determine for each daily measurement and each channel a reference 'Rayleigh'
468           zone $z_{ref}$ supposed free of any aerosols.
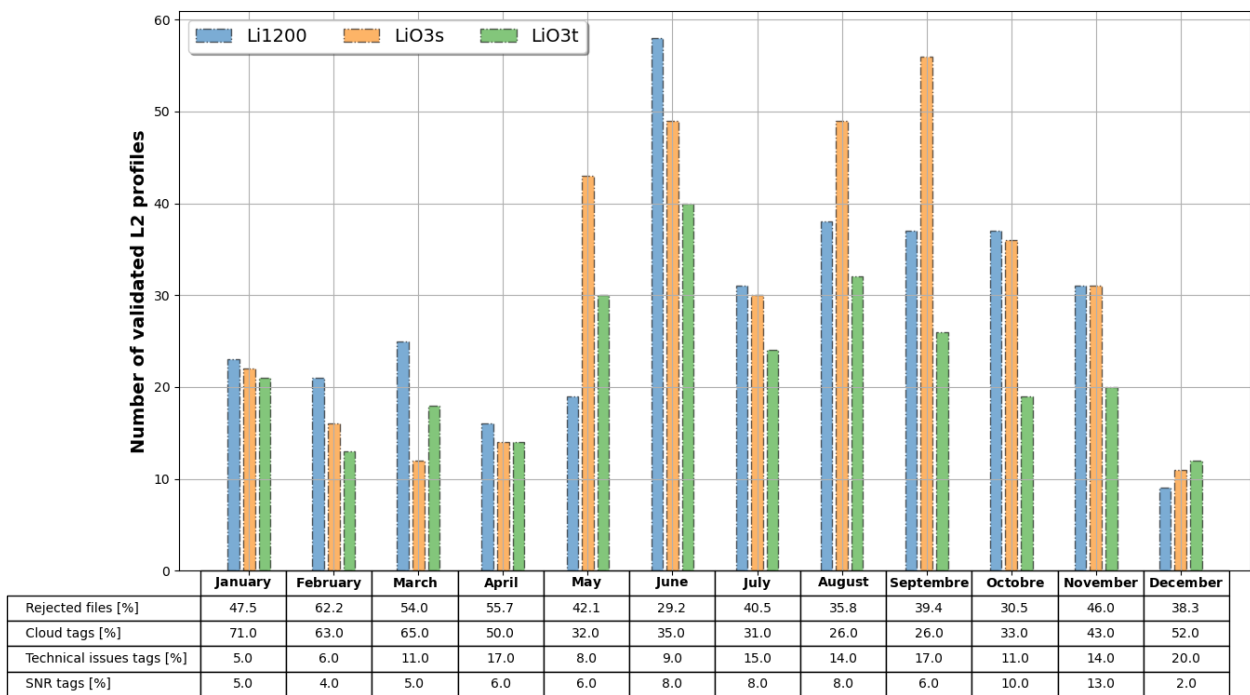
### 4.3.8. Raman and 1064 nm channel issues

Klett inversion brings the problem of considering a lidar ratio constant with height. In fact, a single aerosol plume is often made of several layers of particles with heterogenous backscattered lidar signals. Raman inversion is one solution to deduce a vertical profile of lidar ratio from elastic and Raman channels. However, our Raman channels have a poor SNR and are not usable for stratospheric or high tropospheric aerosols. The retrieval of aerosol optical products using Raman inversion for low-energy channels (low and middle troposphere) is still ongoing. There is also a misalignment issue for the 1064-nm channel leading to a poor SNR. This channel is currently unexploitable.

## 5. Quality assessment

### 5.1. Database statistics

A total of 1737 nighttime measurements were preprocessed between 2013 and 2023: 710 files for Li1200, 534 files for LiO3S, and 493 files for LiO3T. Notably, the mean percentage of rejected files was higher for Li1200 (52.7%), than LiO3T (44.8%) and LiO3S (32.7%). **Figure 8** shows the cumulated monthly number of validated $L_2$ profiles for each instrument, the monthly mean number of rejected files and corresponding tags (cloud detection, technical issue, low SNR). It should be noted that most observations were made during the May to November period (austral winter, dry season) compared to the December to April period (austral summer, wet season), which is consistent with the higher cloud and rain occurrence during the wet season. The mean percentage of validated $L_1$ files was 62.4% during the dry season and 48.5% during the wet season. The lower frequency of measurements in January, July, August, and December also concurs with two important holiday periods. The frequency of technical issues and lower SNR is statistically higher during the months with a greater number of measurements.



| | January | February | March | April | May | June | July | August | Septembre | Octobre | November | December |
|---|---|---|---|---|---|---|---|---|---|---|---|---|
| Rejected files [%] | 47.5 | 62.2 | 54.0 | 55.7 | 42.1 | 29.2 | 40.5 | 35.8 | 39.4 | 30.5 | 46.0 | 38.3 |
| Cloud tags [%] | 71.0 | 63.0 | 65.0 | 50.0 | 32.0 | 35.0 | 31.0 | 26.0 | 26.0 | 33.0 | 43.0 | 52.0 |
| Technical issues tags [%] | 5.0 | 6.0 | 11.0 | 17.0 | 8.0 | 9.0 | 15.0 | 14.0 | 17.0 | 11.0 | 14.0 | 20.0 |
| SNR tags [%] | 5.0 | 4.0 | 5.0 | 6.0 | 6.0 | 8.0 | 8.0 | 8.0 | 6.0 | 10.0 | 13.0 | 2.0 |

**Figure 8: Number of validated files for the three instruments in the period 2013-2023. In the table below, mean percentage of rejected files and tagged files for each month.**
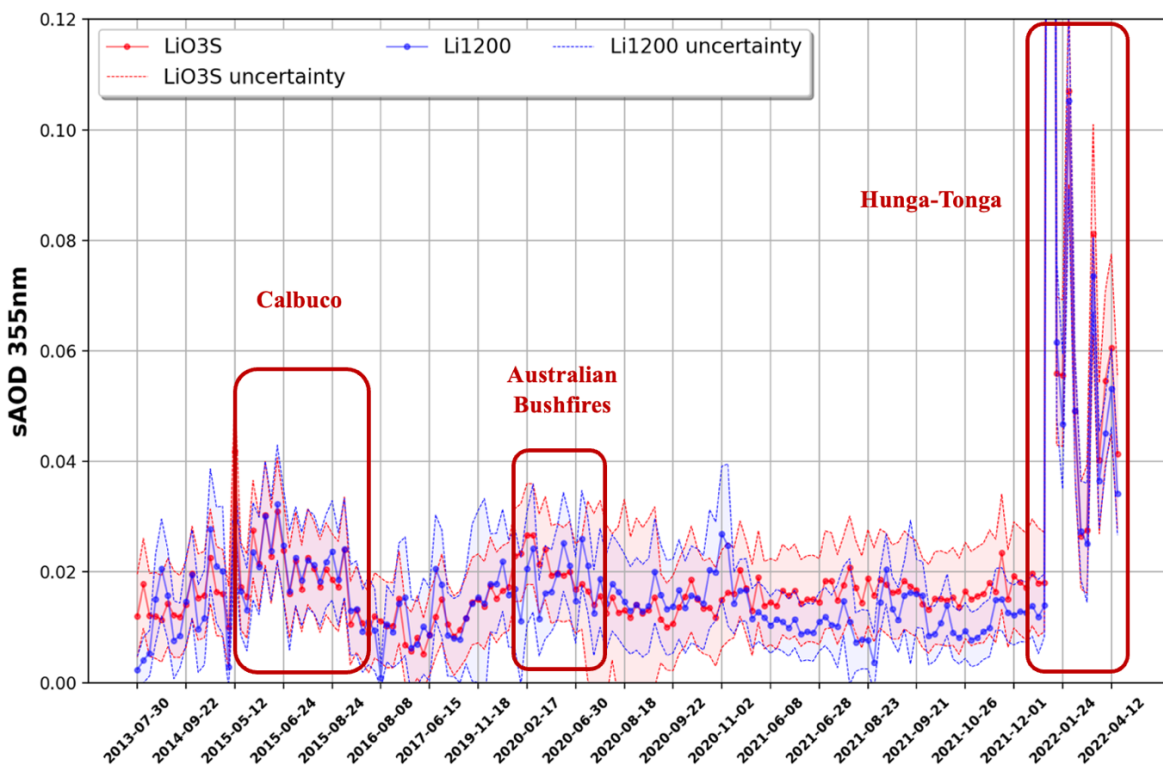
## 5.2. Instrumental capabilities

The gluing technique allowed to determine different altitude ranges for each lidar depending on the channels available. **Table 1** provides a summary of the theoretical instrumental performances in terms of altitude ranges. Apart from the number of glued channels, other parameters can influence the maximum altitude (SNR) or the minimum altitude (Overlap, SNR) of the validated $L_2$ vertical profile. The LiO3T at 532 nm is ideal to investigate the low and mid troposphere. The high troposphere and stratosphere can be studied at 355 nm (Li1200 and LiO3S) or 532 nm (LiO3T – from 2017 until now).
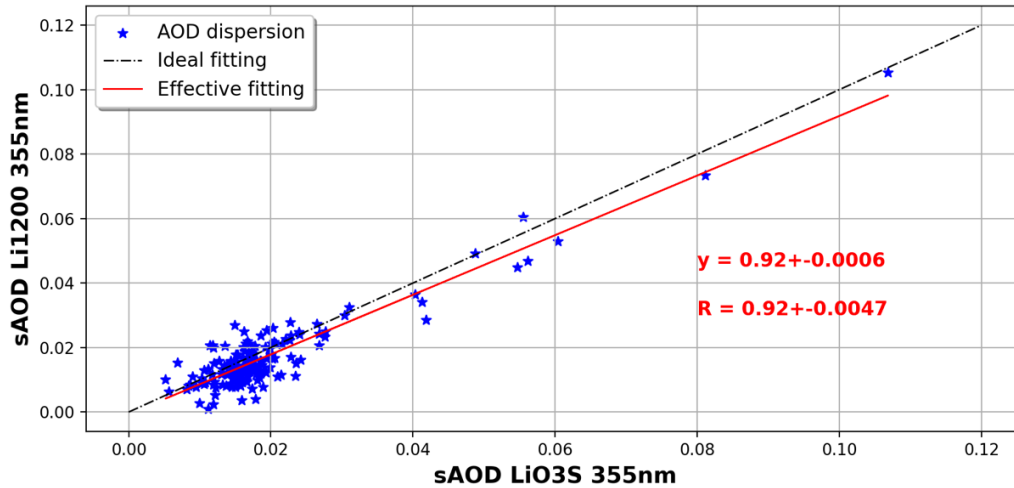
## 5.3. Instrumental intercomparison

In this study, we performed a comparison between the three instruments to detect any major discrepancies using the Stratospheric Aerosol Optical Depth (sAOD) between 17 and 30 km. **Figure 9** displays the time-series of sAOD at 355 nm (Li1200 and Li03S) for concomitant measurements and corresponding uncertainties. There is a good overall consistency between the two instruments. The differences between the two time-series could be the consequence of technical modifications (channel addition, optimization, misalignments). Three peaks periods of high sAOD values can be identified: the emission of volcanic aerosols in the stratosphere during the Hunga-Tonga eruption in 2022 (Kloss et al., 2022; Baron et al., 2023; Sicard et al., 2024), the Calbuco volcanic eruption in 2015 (Bègue et al., 2017) and the Australian bushfires in 2020 ( Khaykin et al., 2020). Higher differences in 2021 could be the consequence of repeated misalignments for the Li1200.



**Figure 9: Nighttime AOD (17 to 30 km layer) at 355 nm, from the Li1200 (red) and LiO3S (blue) (concurrent measurements) with corresponding uncertainties (dashed colored lines). Exceptional events circled in red. The horizontal timeline is not linear: one date out of eight is represented for visual purposes.**

The dispersion of sAOD values is represented in **Figure 10**. The sAOD at 355 nm varies between 0.001 and 0.107 for LiO3S and Li1200, with a mean of $0.019 \pm 0.012$ and $0.017 \pm 0.012$, respectively. A good correlation is found between the two lidars (correlation R = $0.924 \pm 0.005$).
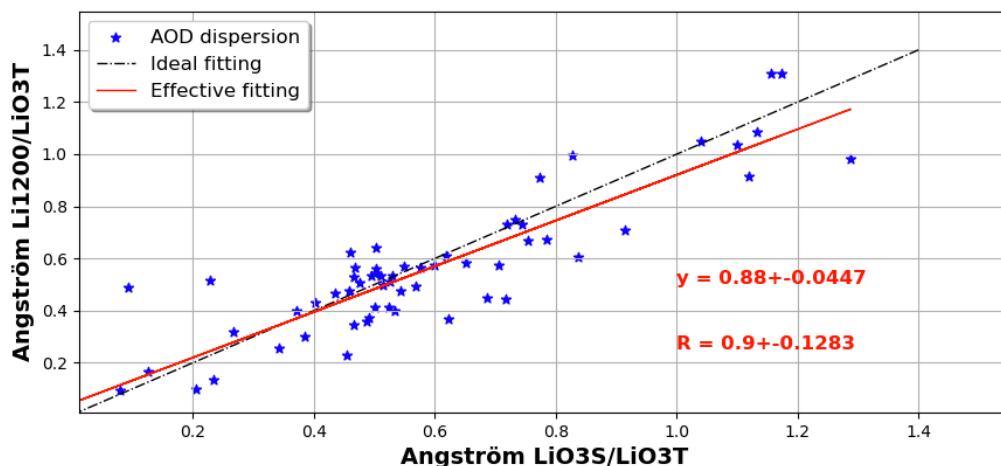
**Figure 10: Dispersion of the AOD (17 to 30 km layer) at 355 nm, between the Li1200 and LiO3S. The red line represents the theoretical linear regression.**

The correlation between the two instruments at 355 nm in terms of extinction values is higher above 17 km but lower from 10 to 17 km (**Appendix D**, **Figure D1**). In fact, for the Li1200: **(i)** low energy channels were added in 2017, **(ii)** there were changes in the minimal altitude of detection for the 355M channel, and **(iii)** this instrument had many misalignments and underwent several optical upgrades, leading to modifications of the overlap function.

For further retrospective trend studies, it is important to note that the LiO3S has been the most stable instrument throughout the time-series and is considered the reference instrument at 355 nm. However, data from the Li1200 can be used to fill the gaps of the LiO3S database depending on the altitude range targeted, but also for specific case studies with the need to retrieve optical products for the middle and low troposphere.

The same analysis was performed for the LiO3T. To compare the two wavelengths, Ångström exponents (AE) were computed between the LiO3T (532 nm) and alternatively the LiO3S (355 nm) and Li1200 (355 nm). **Figure 11** shows the dispersion of AE values. The order of magnitude of AE values varies between 0.0794 and 1.288 with a mean of $0.56 \pm 0.29$ and $0.54 \pm 0.28$, respectively. Again, a good correlation is found between both datasets ($R = 0.901 \pm 0.128$). These values also demonstrate the variability of stratospheric aerosol size distribution between 17 and 30 km (Gobbi et al., 2007; Burton et al., 2012).



**Figure 11: Dispersion of the AE (17 to 30 km layer) between 355 and 532 nm. The black line represents the theoretical linear regression and the red line the actual linear regression.**

19

532   **Table 2** summarizes the metrics used to intercompare the three instruments. The relative Mean Bias Error (MBE)

533   was added the analysis. After identifying the LiO3S as the reference instrument at 355 nm, we found a negative

534   MBE (- 6.55 %) concerning sAOD, meaning that the Li1200 tends to underestimate sAOD compared to LiO3S.

| | Relative Mean Bias Error | Linear Regression Slope | Correlation coefficient |
|---|---|---|---|
| **sAOD** | - 7.59 % | 0.92 | 0.92 ± 0.0047 |
| **Ångström exponent** | - 6.55 % | 0.88 | 0.90 ± 0.1283 |

535   **Table 2: Intercomparison between the three instruments in terms of sAOD and Ångström exponent.**

536   ### 5.4.    Main sources of uncertainties

537   The total uncertainty budget of each lidar is described in **Appendix B**. Four sources of uncertainty were

538   propagated in quadrature (Sicard et al., 2009; Rocadenbosch et al., 2010): **(i)** uncertainty due to the Rayleigh

539   calibration value ($u_{altref}$), **(ii)** uncertainty due to the lidar ratio value ($u_{LR}$) with a distinction between *LR, top* and

540   *LR, bottom* defining the respective upper and lower error bars, **(iii)** uncertainty due to the SNR vertical distribution

541   ($u_{SNR}$), **(iv)** and uncertainty due to the SNR value at the calibration altitude ($u_{SNR,altref}$). **Figures 12a-12c**

542   represent for three case reports the importance of each uncertainty relatively to the total backscatter in percentage**,**

543   and **Figures 12d-12f** represent the corresponding propagated total backscatter uncertainty for the three

544   instruments.

545   In **Figures 12a-12c,** the behavior of the uncertainties $u_{altref}$ (blue curves) and $u_{SNR,altref}$ (green curves) is

546   stable over the different altitude ranges. Notably, $u_{altref}$ comes from the 5% uncertainty of the molecular

547   backscatter, which determines the lower threshold for the total uncertainty. The $u_{SNR}$ uncertainty (purple curves)

548   is strongly influenced by the altitude, with minimal values at lower altitude ranges where the lidar signal is stronger,

549   and values increasing with the altitude. In fact, lidar signals are filtered before inversion, making $u_{SNR}$ the

550   predominant error at higher altitude levels. Oppositely, the $u_{LR}$ uncertainty (orange and yellow curves) is the lowest

551   at the calibration altitude and increases in the lower levels, where it becomes predominant. The systematic

552   uncertainty on the LR value was set to 30% for this study. Therefore, the total uncertainty is the lowest in mid-

553   altitude ranges before increasing in lower and higher altitude levels. Sharp spikes in $u_{LR}$ can be observed just

554   below 20km for the LiO3S and Li1200, and below 8 km for the LiO3T. They are linked to the presence of aerosol

555   plumes and emphasize the impact of aerosols on the uncertainty values in lower altitude levels.

556   For the LiO3S (H+M glued channel), the total relative uncertainty reaches 15% at 10 km, decreases down to

557   6% around 20 km, and increases up to 8% around 35 km. (**Figure 12a**). Without the aerosol layer, the minimum

558   error would be reached around 15 km. For the Li1200 (H+M+L+VL glued channel), the total relative uncertainty

559   reaches 20% at 7 km and decreases down to 5% from 20 km up. (**Figure 12b**). The uncertainty due to the SNR is

560   very low compared to the LiO3S, as this instrument is designed to reach very high-altitude levels, and the signal

561   used for inversion is made of four filtered signals with complementary vertical capacities. Without the aerosol

562   layer, the minimum error would be reached around 17 km. For the LiO3T, the total relative reaches 10% at 4 km,

563   decreases down to 6% around 8 km, and increases up to 20% around 25 km. (**Figure 12c**). The uncertainty due to

564   the SNR is higher than the previous lidars because this instrument is designed for tropospheric measurements.

565

566
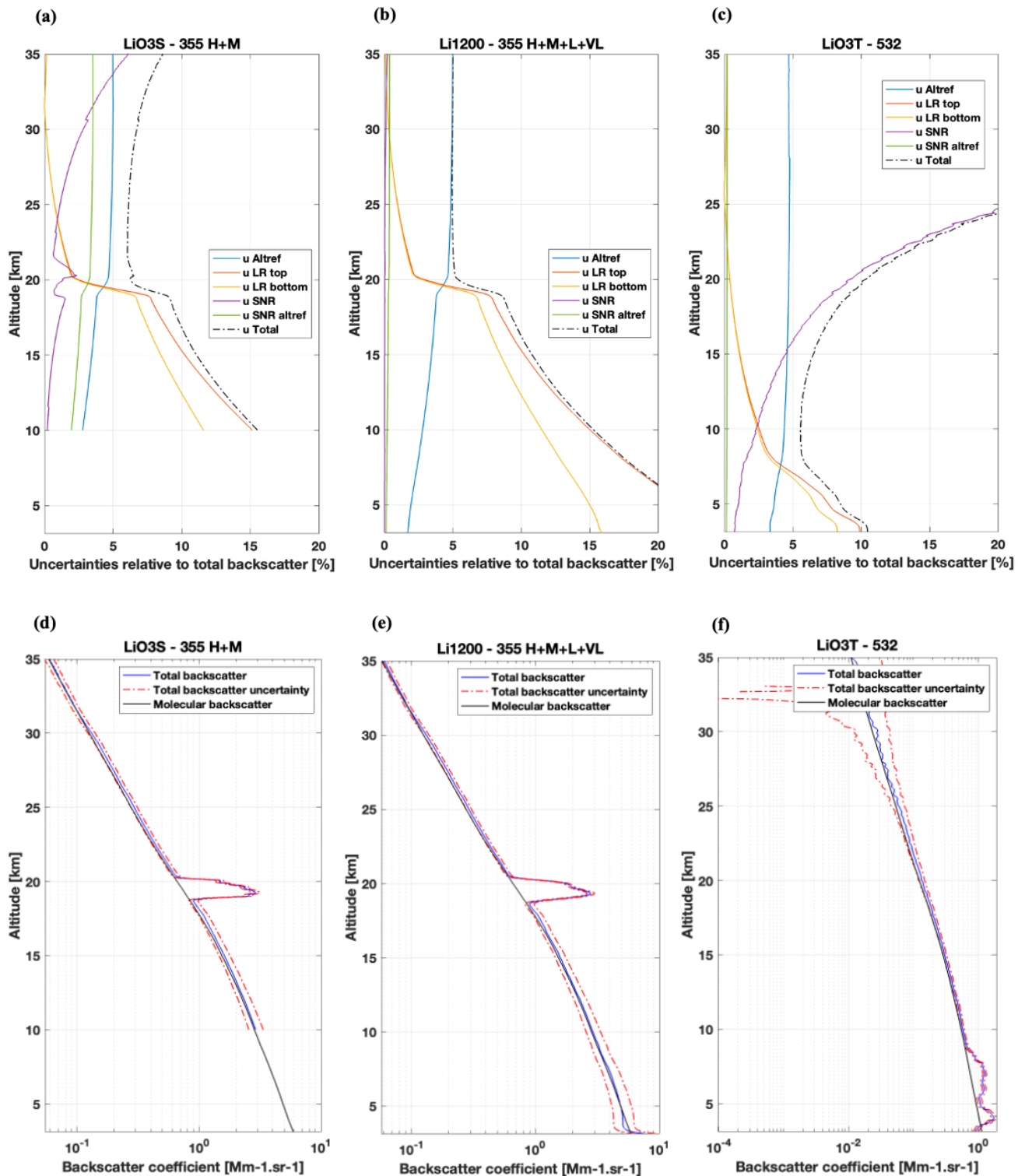
**Figure 12: Upper row: random cases showing the molecular backscatter (black), the backscatter coefficient (blue) and its apparent uncertainty (red dotted line) for the (a) LiO3S (25/01/2022), (b) Li1200 (25/01/2022) and (c) LiO3T (25/09/2017). Lower row: corresponding relative uncertainties for the (d) LiO3S, (e) Li1200 and (f) LiO3T.**

In **Figures 12d-12f**, the three instruments demonstrate their capacity to detect aerosol layers with relatively low error rates and a high resolution. **Figures 12d-12e** specifically show their ability to identify variations within the aerosol layer between 18 and 20 km. For the LiO3T (**Figures 12f**), the aerosol layer between 4 and 8 km is exceptionally well defined, with relatively low error values. Apart from these aerosol layers, the molecular backscatter (in black) tends to align closely with the uncertainty of the total backscatter (in red). In fact, background

21

aerosols are characterized by very low backscatter and extinction values, leading to the relatively high sAOD uncertainties observed in **Figure 9**: higher for background aerosols but lower for cases with a stronger aerosol load, such as from Australian fires or volcanic aerosols. Focusing on the uncertainty specific to aerosol backscatter (rather than the total) is essential to improve the uncertainty analysis, along with a statistical analysis of the dataset to minimize disruptions caused by transient aerosol events. Time-series of aerosol backscatter relative total uncertainties were computed for the three instruments and the corresponding mean and standard deviation are represented **Figures 13a-c**. Values are high and easily reach 100% for the three instruments because of the very low values of aerosol backscatter coefficients above Maïdo observatory. The mean uncertainty is the lowest for the LiO3S between 18 and 25 km (64.4$\pm$ 31.6 %). It increases under 18 km and above 25 km with relative uncertainty values reaching more than 100% due to the very weak aerosol backscatter values at these altitude ranges. The mean uncertainty for the Li1200 is also the lowest between 18 and 25 km (50.3 $\pm$ 29.0 %). It increases under 18 km and above 25 km with relative uncertainty values relatively lower than the LiO3S due to a lower SNR, and the presence of low and very low channels detecting aerosol plumes at lower altitudes. The LiO3T exhibits a low relative uncertainty below 20 km, it varies around 69.1 $\pm$ 42.7 %. The strong increase above 20 km is essentially explained by the very low SNR for this instrument at these altitude ranges.
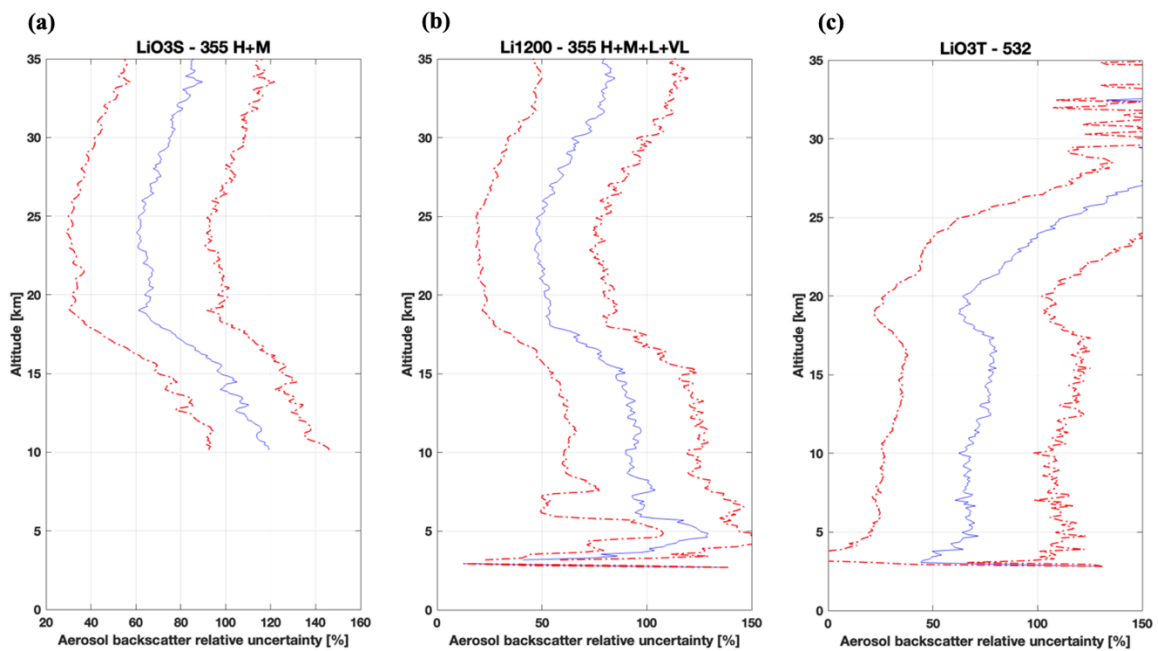


**Figure 13: Mean (blue line) and standard deviation (dotted red line) of the time-series of relative uncertainty from the inversion technique for the (a) lidar O3S (H+M channel), (b) lidar 1200 (H+M+L+VL channel) and (c) lidar O3T (polarized channels).**

**Table 3** provides a summary of the processing method and the area of validity of the Level 2 products.

| | Li1200 | | LiO3S | LiO3T | |
|---|---|---|---|---|---|
| **Time-series** | In 2013-2017 | 2017-ongoing | 2013-current | In 2013-2017 | 2017-ongoing |
| **Elastic reception channels (nm)** | 355H, 355M | + 355L, 355VL | 355H, 355M | Elastic // 532 Elastic ⊥ 532 | + 532H |
| **Geometrical form factor correction method** | - | From vertical measurements | - | - | - |
| **Polarization calibration method** | - | | - | Rayleigh method | 3 signals method |
| **Inversion method** | Klett | | | | |
| **Vertical resolution range (km)** | 0.030 – 0.522 | 0.015 – 0.522 | 0.030 – 0.261 | 0.052 – 0.522 | |
| **Detection lower bound (km)** | 10 | 3 | 10 | 3 | 10 |
| **Detection upper bound (km)** | 45 | 45 | 40 | 25 | 35 |
| **Uncertainty averaged lowest values (%)** | $50.3 \pm 29.0$ | | $64.4 \pm 31.6$ | $69.1 \pm 42.7$ | |

**Table 3: Summary of the processing method and area of validity for the Level 2 products.**

## 6. Data availability

Raw $L_0$ files, cleaned $L_1$ files and processed $L_2$ files with optical products are generated locally. $L_0$ files are made of 1minute integrated raw files in licel format. $L_1$ products contain 1-minute integrated time-series and overnight averaged cleaned signals in mat file format and netcdf format. $L_2$ products in mat file format contain overnight averaged processed signals, as well as range-corrected signals for Raman channels. $L_2$ products are also computed in netcdf format following NDACC guidelines in anticipation for a future NDACC label request. **Table C1** in **Appendix C** summarizes the optical products and other variables available in these $L_2$ netcdf files.

Each of these files is available on request in our local datacenter by FTP (ftp://tramontane.univ-reunion.fr/). $L_1$ and $L_2$ files are currently available at https://doi.org/10.26171/rwcm-q370 (Gantois et al., 2024). Mat files and netcdf files with $L_2$ data will soon be available on AERIS database, but only $L_2$ netcdf files will be openly accessible.

## 7. Summary

This study supports the first ever long-term time-series of multiwavelength aerosol optical properties generated from three lidars operating at the Observatory of Atmospheric Physics of La Réunion (OPAR) since 2013. A full description of the technical specifications for the three instruments is provided, as well as details about the preprocessing and processing methods used to produce the different dataset levels. The three time-series consist in vertical profiles of aerosol elastic backscatter and extinction coefficients at 355 and 532 nm, and linear depolarization ratio at 532 nm above Maïdo observatory (2160 m asl, west side of Reunion Island, Southern Hemisphere) from 2013 until now.

The preprocessing step required manual cleaning of more than 1700 files, and the highest frequency of cloud occurrence resulted in a lower number of validated profiles during the wet season. Data processing methods and the Klett inversion technique chosen for this work are detailed and referenced. One issue concerns the random misalignments and technical modifications for the three instruments leading to highly variable parameters such as the geometrical form factor. As an alternative to the Klett method, the Raman inversion technique has been attempted but failed for stratospheric and high tropospheric levels due to a poor SNR.

630    Intercomparison between the three instruments show a good correlation in terms of sAOD values. The
631    uncertainty analyses reveal a strong influence of the LR value in the low-altitude ranges and a strong influence of
632    the SNR in the high-altitude ranges. Uncertainty values relative to the total backscatter coefficient are low for the
633    three instruments. Uncertainty values relative to the aerosol backscatter coefficient are high for the three
634    instruments because of the very low aerosol backscatter coefficient values generally observed above Maïdo
635    observatory. Among the three instruments, the LiO3S stands out as the most stable (less misalignments, less
636    technical modifications) and should be considered the reference instrument at 355 nm. However, data from the
637    Li1200 can be used to fill the gaps of the LiO3S database and for specific case studies.

638    **Appendices**

639    **Appendix A**

640    The equation describing the desaturated lidar signal can be written as:

641
$$S_{desat}(\lambda, z) = C(\lambda) \cdot \frac{F(z)}{(z-z_0)^2} \cdot \left\{ \sum_i \beta_i(\lambda, z) \right\} \cdot \left\{ exp\left[ -\frac{2}{\cos(\theta)} \cdot \sum_i \tau_i(\lambda, z_0, z) \right] \right\} + S_{bck}(\lambda) \quad (A1)$$

642    With $C$ the instrumental constant, $F$ the overlap function, $\beta_i$ the backscatter coefficient of the component $i$, $\tau_i$ the
643    integrated extinction coefficient of the component $i$ between altitude $z_0$ and $z$, and $S_{bck}$ the background signal.

644    The range-corrected, sky background corrected and desaturated signal can then be considered:

645

646
$$S_2(\lambda, z) = [S_{desat}(\lambda, z) - S_{bck}(\lambda, z)] \cdot (z - z_0)^2 \quad (A2)$$

647

648    Derivation of the logarithm of $S_2$ leads to:

649

650
$$\frac{\delta[ln(S_2)]}{\delta z} = \frac{1}{\beta(\lambda, z)} \cdot \frac{\delta[\beta(\lambda, z)]}{\delta z} - 2 \cdot LR_a(\lambda, z) \cdot \beta(\lambda, z) - 2 \cdot \alpha_m(\lambda, z) \cdot \left( 1 - \frac{LR_a(\lambda, z)}{LR_m} \right) \quad (A3)$$

651

652    With $a$ (resp. $m$) the particular (resp. molecular) contribution, $\alpha(\lambda, z)$ (resp. $\beta(\lambda, z)$) the summed molecular and
653    particular extinction (resp. backscatter), and $LR$ the Lidar Ratio:

654
$$LR_a(\lambda, z) = \frac{\alpha_a(\lambda, z)}{\beta_a(\lambda, z)} \quad (A4)$$

655
$$LR_m(\lambda, z) = \frac{\alpha_m(\lambda, z)}{\beta_m(\lambda, z)} = \frac{8\pi}{3} * K_f \quad (A5)$$

656    With $K_f$ corresponding to the King factor's value.

657    The two-component solution of this Bernoulli equation is:

658

659  $$\beta(\lambda, z) = \beta_a(\lambda, z) + \beta_m(\lambda, z)$$

660  $$= \frac{S_2(\lambda, z) \cdot \exp\{2 \cdot \int_{z'=z}^{z_{ref}} \left(\frac{LR_a(\lambda, z')}{LR_m(\lambda, z')} - 1\right) \cdot \alpha_m(\lambda, z') dz'\}}{\frac{S_2(\lambda, z_{ref})}{\beta(\lambda, z_{ref})} + 2 \cdot \int_{z'=z}^{z_{ref}} LR_a(\lambda, z') \cdot S_2(\lambda, z') \cdot \exp\{2 \cdot \int_{x'=z}^{z_{ref}} \left(\frac{LR_a(\lambda, x')}{LR_m(\lambda, x')} - 1\right) \cdot \alpha_m(\lambda, x') dx'\} \cdot dz'} \quad (A6)$$

661

662  **Appendix B**

663  The uncertainty budget was determined from the Klett elastic one components inversion technique. Mathematical

664  details can be found in (Rocadenbosch et al., 2010) for the total backscatter inversion uncertainty budget and

665  (Sicard et al., 2009) for the two components inversion uncertainty budget.

666  The Klett inversion was applied to the filtered signal following (see section 4.3.4.):

667  $$S_{filt}(z) = \frac{S_2(z)}{F(z)} * \frac{coef}{\sum coef} \quad (3)$$

668  Considering $C = \frac{coef}{\sum coef}$ and $S_{geo}(z) = \frac{S_2(z)}{F(z)}$, the uncertainty of the filtered signal followed the equation:

669  $$u_{filt}(z) = \sqrt{\left[\frac{\partial S_{filt}(z)}{\partial S_{geo}(z)} \cdot u_{S_{geo}}(z)\right]^2 + \left[\frac{\partial S_{filt}(z)}{\partial C} \cdot u_C(z)\right]^2} = \sqrt{\left[C(z) \cdot u_{S_{geo}}(z)\right]^2 + \left[S_{geo}(z) \cdot u_C(z)\right]^2} \quad (B1)$$

670

671  **Table B1** is a summary of the Total-Backscatter analytical error bars to compute in Klett's backward inversion

672  method.

| Uncertainty source | Equation |
|---|---|
| Uncertainty due to the Rayleigh calibration value ($u_{altref}$) | $u_{altref} = \left\|\left(\frac{\beta_j}{\beta_N}\right)^2 \frac{U_N}{U_j}\right\| \sigma_{\beta_N}$ |
| Uncertainty due to the lidar ratio value ($u_{LR}$) | $u_{LR} = \left\|\pm p \frac{2\beta_j^2}{U_j} G_j + p^2 \frac{4\beta_j^3}{U_j^2} G_j{}^2\right\|$ <br> Where: $G_j = \sum_{i=j}^N w_i S_i U_i$ |
| Uncertainty due to the SNR vertical distribution ($u_{SNR}$). | $u_{SNR} = \sqrt{\left(\frac{\beta_j}{U_j}\right)^2 \sigma_{U_j}^2 + \left(\frac{2\beta_j}{U_j}\right)^2 \sigma_{GU_j}^2}$ <br> Where: $\sigma_{GU_j}^2 = \sum_{k=j}^N (w_k S_k)^2 \sigma_{U_k}{}^2$ |
| Uncertainty due to the SNR value at the calibration altitude ($u_{SNR,altref}$). | $u_{SNR,altref} \approx \left\|\frac{\beta_j^2}{\beta_N U_j}\right\| \sigma_{U_N}$ |

673  **Table B1: Total-Backscatter analytical error bars from Klett's backward inversion method (from Rocadenbosch et al.,**
674  **2010)**

675

676  With $\beta_j$ the total backscatter at the altitude cell j, $U_j$ the range-corrected signal at the altitude cell j, N the calibration

677  altitude cell, $\sigma_{U_j}$ the uncertainty if the range-corrected signal U, $\sigma_{\beta_j}$ the uncertainty of the total backscatter, $S_j$ the

678  total lidar ratio.

679  The uncertainty of the total backscatter error bars $u_{\beta T}$ can then be written as:

680

$$u_{\beta T} = \sqrt{u_{altref}^2 + u_{LR}^2 + u_{SNR}^2 + u_{SNR,altref}^2} \quad (B2)$$

681

| Variable | Dimension | Unit |
|---|---|---|
| **CHANNELS_ID** | channel | - |
| **LATITUDE_INSTRUMENT** | time | deg |
| **LONGITUDE_INSTRUMENT** | time | deg |
| **STATION_HEIGHT** | time | m_asl |
| **DATETIME** | time | MJD2K |
| **DATETIME_START** | time | MJD2K |
| **DATETIME_STOP** | time | MJD2K |
| **INTEGRATION_TIME** | time | h |
| **WAVELENGTH_EMISSION** | channel | nm |
| **WAVELENGTH_DETECTION** | channel | nm |
| **ANGLE_VIEW_ZENITH** | time, channel | deg |
| **ACCUMULATED_LASER_SHOTS** | time, channel | 1 |
| **ALTITUDE** | points | m_asl |
| **AEROSOL_RETRIEVAL_METHOD** | time | - |
| **AEROSOL_BACKSCATTER_RATIO_BACKSCATTER** | time, channel, points | 1 |
| **AEROSOL_BACKSCATTER_RATIO_BACKSCATTER_UNCERTAINTY_COMBINED_STANDARD** | time, channel, points | 1 |
| **AEROSOL_BACKSCATTER_RATIO_BACKSCATTER_RESOLUTION_ALTITUDE_IMPULSE_RESPONSE_FWHM** | time, channel, points | m |
| **RANGE_INDEPENDENT_NORMALIZATION** | time | m_asl |
| **RANGE-CORRECTED_SIGNAL** | time, channel, points | Photons.s-1 |
| **AEROSOL_BACKSCATTER_COEFFICIENT_DERIVED** | time, channel, points | m-1.sr-1 |
| **AEROSOL_BACKSCATTER_COEFFICIENT_DERIVED_UNCERTAINTY_COMBINED_STANDARD** | time, channel, points | m-1.sr-1 |
| **AEROSOL_BACKSCATTER_COEFFICIENT_DERIVED_RESOLUTION_ALTITUDE_IMPULSE_RESPONSE_FWHM** | time, channel, points | m |
| **PRESSURE_INDEPENDENT** | points | hPa |
| **TEMPERATURE_INDEPENDENT** | points | K |
| **AEROSOL_EXTINCTION_COEFFICIENT_DERIVED** | time, channel, points | m-1 |
| **AEROSOL_ EXTINCTION _COEFFICIENT_DERIVED_UNCERTAINTY_COMBINED_STANDARD** | time, channel, points | m-1 |
| **AEROSOL_ EXTINCTION _COEFFICIENT_DERIVED_RESOLUTION_ALTITUDE_IMPULSE_RESPONSE_FWHM** | time, channel, points | m |
| **AEROSOL_LIDAR_RATIO_INDEPENDENT** | time, channel, points | sr |
| **VOLUME_LINEAR_DEPOLARIZATION_RATIO** | time, channel, points | 1 |
| **VOLUME_LINEAR_DEPOLARIZATION_RATIO _UNCERTAINTY_COMBINED_STANDARD** | time, channel, points | 1 |
| **VOLUME_LINEAR_DEPOLARIZATION_RATIO _RESOLUTION_ALTITUDE_IMPULSE_RESPONSE_FWHM** | time, channel, points | m |
| **AEROSOL_LINEAR_DEPOLARIZATION_RATIO_DERIVED** | time, channel, points | 1 |
| **AEROSOL_LINEAR_DEPOLARIZATION_RATIO_DERIVED _UNCERTAINTY_COMBINED_STANDARD** | time, channel, points | 1 |
| **AEROSOL_LINEAR_DEPOLARIZATION_RATIO_DERIVED _RESOLUTION_ALTITUDE_IMPULSE_RESPONSE_FWHM** | time, channel, points | m |

**Table C1: Variables available in the L$_2$ netcdf files**

**Appendix D**
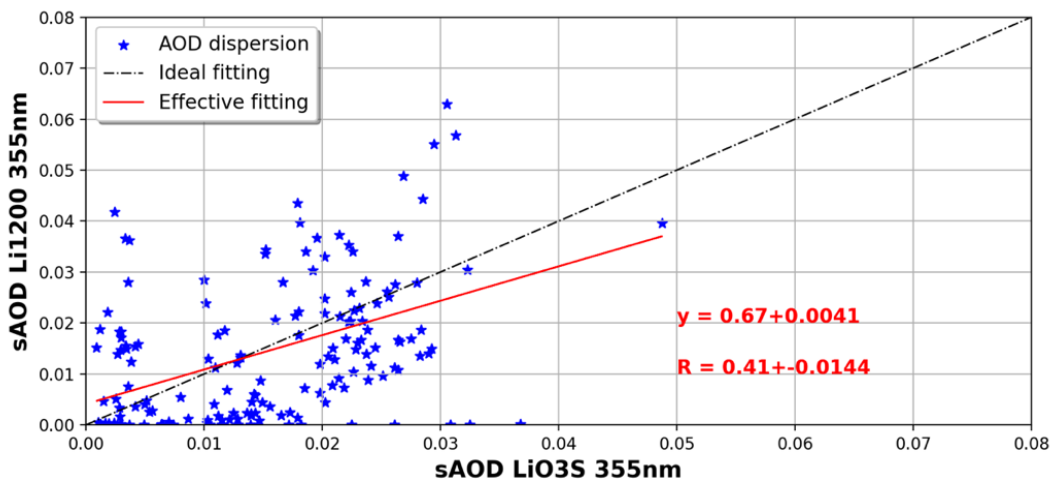
**Figure D1: Dispersion of the AOD (10 to 17 km layer) at 355 nm, between the Li1200 and LiO3S. The black line represents the theoretical linear regression and the red line the actual linear regression.**

**References**

Alexander, L., Allen, S., Bindoff, N., Breon, F.-M., Church, J., Cubasch, U., Emori, S., Forster, P., Friedlingstein, P., Gillett, N., Gregory, J., Hartmann, D., Jansen, E., Kirtman, B., Knutti, R., Kanikicharla, K., Lemke, P., Marotzke, J., Masson-Delmotte, V., and Xie, S.-P.: Climate change 2013: The physical science basis, in contribution of Working Group I (WGI) to the Fifth Assessment Report (AR5) of the Intergovernmental Panel on Climate Change (IPCC), in: Climate Change 2013: The physical science basis, 2013.

710  Ansmann, A., Riebesell, M., and Weitkamp, C.: Measurement of atmospheric aerosol extinction profiles with a
711  Raman lidar, Opt. Lett., 15, 746, https://doi.org/10.1364/OL.15.000746, 1990.

712  Ansmann, A., Wandinger, U., Riebesell, M., Weitkamp, C., and Michaelis, W.: Independent measurement of
713  extinction and backscatter profiles in cirrus clouds by using a combined Raman elastic-backscatter lidar, Appl.
714  Opt., 31, 7113, https://doi.org/10.1364/AO.31.007113, 1992.

715  Baray, J.-L., Courcoux, Y., Keckhut, P., Portafaix, T., Tulet, P., Cammas, J.-P., Hauchecorne, A., Godin-
716  Beekmann, S., De Mazière, M., Hermans, C., Desmet, F., Sellegri, K., Colomb, A., Ramonet, M., Sciare, J.,
717  Vuillemin, C., Hoareau, C., Dionisi, D., Duflot, V., Vérèmes, H., Porteneuve, J., Gabarrot, F., Gaudo, T., Metzger,
718  J.-M., Payen, G., Leclair De Bellevue, J., Barthe, C., Posny, F., Abchiche, A., Delmas, R., and Ricaud, P.: Maïdo
719  observatory: a new high-altitude station facility at Reunion Island (21° S, 55° E) for long-term atmospheric remote
720  sensing and in situ measurements, Atmospheric Meas. Tech., 6, 2865–2877, https://doi.org/10.5194/amt-6-2865-
721  2013, 2013.

722  Baron, A., Chazette, P., Khaykin, S., Payen, G., Marquestaut, N., Bègue, N., and Duflot, V.: Early Evolution of
723  the Stratospheric Aerosol Plume Following the 2022 Hunga Tonga-Hunga Ha'apai Eruption: Lidar Observations
724  From Reunion (21°S, 55°E), Geophys. Res. Lett., 50, e2022GL101751, https://doi.org/10.1029/2022GL101751,
725  2023.

726  Bates, D. R.: Rayleigh scattering by air, Planet. Space Sci., 32, 785–790, https://doi.org/10.1016/0032-
727  0633(84)90102-8, 1984.

728  Bègue, N., Vignelles, D., Berthet, G., Portafaix, T., Payen, G., Jégou, F., Benchérif, H., Jumelet, J., Vernier, J.-P.,
729  Lurton, T., Renard, J.-B., Clarisse, L., Duverger, V., Posny, F., Metzger, J.-M., and Godin-Beekmann, S.: Long-
730  range transport of stratospheric aerosols in the Southern Hemisphere following the 2015 Calbuco eruption,
731  Atmospheric Chem. Phys., 17, 15019–15036, https://doi.org/10.5194/acp-17-15019-2017, 2017.

732  Behrendt, A. and Nakamura, T.: Calculation of the calibration constant of polarization lidar and its dependency on
733  atmospheric temperature, Opt. Express, 10, 805, https://doi.org/10.1364/OE.10.000805, 2002.

734  Biele, J., Beyerle, G., and Baumgarten, G.: Polarization Lidar: Correction of instrumental effects, Opt. Express, 7,
735  427, https://doi.org/10.1364/OE.7.000427, 2000.

736  Blackman, R. B. and Tukey, J. W.: BSTJ 37: 1. January 1958: The Measurement of Power Spectra from the Point
737  of View of Communications Engineering - Part I. (Blackman, R.B.; Tukey, J.W.), 1958.

738  Burton, S. P., Ferrare, R. A., Hostetler, C. A., Hair, J. W., Rogers, R. R., Obland, M. D., Butler, C. F., Cook, A.
739  L., Harper, D. B., and Froyd, K. D.: Aerosol classification using airborne High Spectral Resolution Lidar
740  measurements – methodology and examples, Atmospheric Meas. Tech., 5, 73–98, https://doi.org/10.5194/amt-5-
741  73-2012, 2012.

742  Cattrall, C., Reagan, J., Thome, K., and Dubovik, O.: Variability of aerosol and spectral lidar and backscatter and
743  extinction ratios of key aerosol types derived from selected Aerosol Robotic Network locations, J. Geophys. Res.
744  Atmospheres, 110, https://doi.org/10.1029/2004JD005124, 2005.

745  Chazette, P., Totems, J., Hespel, L., and Bailly, J.-S.: Principe et physique de la mesure lidar, vol. 1, ISTE, 209,
746  2017.

747  Dionisi, D., Keckhut, P., Courcoux, Y., Hauchecorne, A., Porteneuve, J., Baray, J. L., Leclair de Bellevue, J.,
748  Vérèmes, H., Gabarrot, F., Payen, G., Decoupes, R., and Cammas, J. P.: Water vapor observations up to the lower
749  stratosphere through the Raman lidar during the Maïdo Lidar Calibration Campaign, Atmospheric Meas. Tech., 8,
750  1425–1445, https://doi.org/10.5194/amt-8-1425-2015, 2015.

751  Duflot, V., Baray, J., Payen, G., Marquestaut, N., Posny, F., Metzger, J.-M., Langerock, B., Vigouroux, C., Hadji-
752  Lazaro, J., Portafaix, T., De Maziere, M., Coheur, P.-F., Clerbaux, C., and Cammas, J.-P.: Tropospheric ozone
753  profiles by DIAL at Maïdo Observatory (Reunion Island): System description, instrumental performance and result
754  comparison with ozone external data set, Atmospheric Meas. Tech., 10, 3359–3373, https://doi.org/10.5194/amt-
755  10-3359-2017, 2017.

756  Edwards, D. P., Emmons, L. K., Gille, J. C., Chu, A., Attié, J.-L., Giglio, L., Wood, S. W., Haywood, J., Deeter,
757  M. N., Massie, S. T., Ziskin, D. C., and Drummond, J. R.: Satellite-observed pollution from Southern Hemisphere

biomass burning, J. Geophys. Res., 111, D14312, https://doi.org/10.1029/2005JD006655, 2006.

Freudenthaler, V.: About the effects of polarising optics on lidar signals and the Δ90 calibration, Atmospheric Meas. Tech., 9, 4181–4255, https://doi.org/10.5194/amt-9-4181-2016, 2016.

Gantois, D., Payen, G., Sicard, M., Duflot, V., Marquestaut, N., Portafaix, T., Godin Beekmann, S., Hernandez, P., and Golubic, E.: Multiwavelength aerosol lidars at Maïdo Observatory, https://doi.org/10.26171/rwcm-q370, 2024.

Gobbi, G. P., Kaufman, Y. J., Koren, I., and Eck, T. F.: Classification of aerosol properties derived from AERONET direct sun data, Atmospheric Chem. Phys., 7, 453–458, https://doi.org/10.5194/acp-7-453-2007, 2007.

Godin-Beekmann, S., Porteneuve, J., and Garnier, A.: Systematic DIAL lidar monitoring of the stratospheric ozone vertical distribution at Observatoire de Haute-Provence (43.92°N, 5.71°E), J. Environ. Monit., 5, 57–67, https://doi.org/10.1039/B205880D, 2003.

Hansen, J., Sato, M., and Ruedy, R.: Radiative forcing and climate response, J. Geophys. Res. Atmospheres, 102, 6831–6864, https://doi.org/10.1029/96JD03436, 1997.

Hauchecorne, A.: Ether, Service Arletty, Atmospheric Model Description, ETH-ACR-AR-DM-001, 22 pp., 1998., n.d.

Khaykin, S., Legras, B., Bucci, S., Sellitto, P., Isaksen, L., Tencé, F., Bekki, S., Bourassa, A., Rieger, L., Zawada, D., Jumelet, J., and Godin-Beekmann, S.: The 2019/20 Australian wildfires generated a persistent smoke-charged vortex rising up to 35 km altitude, Commun. Earth Environ., 1, 22, https://doi.org/10.1038/s43247-020-00022-5, 2020.

Khaykin, S. M., Godin-Beekmann, S., Keckhut, P., Hauchecorne, A., Jumelet, J., Vernier, J.-P., Bourassa, A., Degenstein, D. A., Rieger, L. A., Bingen, C., Vanhellemont, F., Robert, C., DeLand, M., and Bhartia, P. K.: Variability and evolution of the midlatitude stratospheric aerosol budget from 22 years of ground-based lidar and satellite observations, Atmospheric Chem. Phys., 17, 1829–1845, https://doi.org/10.5194/acp-17-1829-2017, 2017.

King, L. V.: The Complex Anisotropic Molecule in Relation to the Theory of Dispersion and Scattering of Light in Gases and Liquids, Nature, 111, 667–667, https://doi.org/10.1038/111667a0, 1923.

Klett, J. D.: Stable analytical inversion solution for processing lidar returns, Appl. Opt., 20, 211, https://doi.org/10.1364/AO.20.000211, 1981.

Klett, J. D.: Lidar inversion with variable backscatter/extinction ratios, Appl. Opt., 24, 1638, https://doi.org/10.1364/AO.24.001638, 1985.

Kloss, C., Sellitto, P., Renard, J., Baron, A., Bègue, N., Legras, B., Berthet, G., Briaud, E., Carboni, E., Duchamp, C., Duflot, V., Jacquet, P., Marquestaut, N., Metzger, J., Payen, G., Ranaivombola, M., Roberts, T., Siddans, R., and Jégou, F.: Aerosol Characterization of the Stratospheric Plume From the Volcanic Eruption at Hunga Tonga 15 January 2022, Geophys. Res. Lett., 49, https://doi.org/10.1029/2022GL099394, 2022.

Leblanc, T., Sica, R. J., van Gijsel, J. A. E., Godin-Beekmann, S., Haefele, A., Trickl, T., Payen, G., and Liberti, G.: Proposed standardized definitions for vertical resolution and uncertainty in the NDACC lidar ozone and temperature algorithms – Part 2: Ozone DIAL uncertainty budget, Atmospheric Meas. Tech., 9, 4051–4078, https://doi.org/10.5194/amt-9-4051-2016, 2016a.

Leblanc, T., Sica, R. J., Van Gijsel, J. A. E., Haefele, A., Payen, G., and Liberti, G.: Proposed standardized definitions for vertical resolution and uncertainty inthe NDACC lidar ozone and temperature algorithms – Part 3: Temperatureuncertainty budget, Atmospheric Meas. Tech., 9, 4079–4101, https://doi.org/10.5194/amt-9-4079-2016, 2016b.

Müller, J. W.: Dead-time problems, Nucl. Instrum. Methods, 112, 47–57, https://doi.org/10.1016/0029-554X(73)90773-8, 1973.

Portafaix, T., Morel, B., Bencherif, H., Baldy, S., Godin-Beekmann, S., and Hauchecorne, A.: Fine-scale study of a thick stratospheric ozone lamina at the edge of the southern subtropical barrier, J. Geophys. Res. Atmospheres,

804    108, 2002JD002741, https://doi.org/10.1029/2002JD002741, 2003.

805    Portafaix, T., Godin-Beekmann, S., Payen, G., de Mazière, M., Langerock, B., Fernandez, S., Posny, F., Cammas,
806    J.-P., Metzger, J.-M., Bencherif, H., Vigouroux, C., and Marquestaut, N.: Ozone profiles obtained by DIAL
807    technique at Maïdo Observatory in La Reunion Island: comparisons with ECC ozone-sondes, ground-based FTIR
808    spectrometer and microwave radiometer measurements, in: ILRC 27, 27th International Laser Radar Conference,
809    New-York, United States, 2015.

810    Raut, J.-C. and Chazette, P.: Retrieval of aerosol complex refractive index from a synergy between lidar,
811    sunphotometer and in situ measurements during LISAIR experiment, Atmospheric Chem. Phys., 7, 2797–2815,
812    https://doi.org/10.5194/acp-7-2797-2007, 2007.

813    Reichardt, J., Baumgart, R., and McGee, T. J.: Three-signal method for accurate measurements of depolarization
814    ratio with lidar, Appl. Opt., 42, 4909, https://doi.org/10.1364/AO.42.004909, 2003.

815    Rocadenbosch, F., Md. Reba, M. N., Sicard, M., and Comerón, A.: Practical analytical backscatter error bars for
816    elastic one-component lidar inversion algorithm, Appl. Opt., 49, 3380, https://doi.org/10.1364/AO.49.003380,
817    2010.

818    Sicard, M., Comerón, A., Rocadenbosch, F., Rodríguez, A., and Muñoz, C.: Quasi-analytical determination of
819    noise-induced error limits in lidar retrieval of aerosol backscatter coefficient by the elastic, two-component
820    algorithm, Appl. Opt., 48, 176, https://doi.org/10.1364/AO.48.000176, 2009.

821    Sicard, M., Baron, A. A., Ranaivombola, M., Gantois, D., Millet, T., Sellitto, P., Begue, N., Bencherif, H., Payen,
822    G., Marquestaut, N., and Duflot, V.: Radiative impact of the Hunga Tonga-Hunga Ha'apai stratospheric volcanic
823    plume: role of aerosols and water vapor in the southern tropical Indian Ocean,
824    Preprints, https://doi.org/10.22541/essoar.170231679.99186200/v1, 2024.

825    Tidiga, M., Berthet, G., Jégou, F., Kloss, C., Bègue, N., Vernier, J.-P., Renard, J.-B., Bossolasco, A., Clarisse, L.,
826    Taha, G., Portafaix, T., Deshler, T., Wienhold, F. G., Godin-Beekmann, S., Payen, G., Metzger, J.-M., Duflot, V.,
827    and Marquestaut, N.: Variability of the Aerosol Content in the Tropical Lower Stratosphere from 2013 to 2019:
828    Evidence of Volcanic Eruption Impacts, Atmosphere, 13, 250, https://doi.org/10.3390/atmos13020250, 2022.

829    Vérèmes, H., Payen, G., Keckhut, P., Duflot, V., Baray, J.-L., Cammas, J.-P., Evan, S., Posny, F., Körner, S., and
830    Bosser, P.: Validation of the Water Vapor Profiles of the Raman Lidar at the Maïdo Observatory (Reunion Island)
831    Calibrated with Global Navigation Satellite System Integrated Water Vapor, Atmosphere, 10, 713,
832    https://doi.org/10.3390/atmos10110713, 2019.

833